Rock Mechanics and Rock Engineering
https://doi.org/10.1007/s00603-026-05771-x

ORIGINAL PAPER

Linking Coupled Reservoir Modeling to Dynamic Rupture Modeling: An Automated Workflow to Simulate Induced Seismicity in Faulted Geothermal Systems

Rahim Habibi[1] · Thomas Ulrich[2] · Alice-Agnes Gabriel[2,3] · Thomas Kohl[1] · Emmanuel Gaucher[1]

Received: 19 November 2025 / Accepted: 25 June 2026

Abstract

Induced seismicity associated with subsurface fluid injection poses significant challenges for geothermal reservoir management. While quasi-static models capture long-term pressure, temperature, and stress evolution, dynamic rupture codes resolve transient earthquake mechanics. In this study, we develop a fully coupled framework that integrates both approaches to simulate fault reactivation and induced seismicity in a synthetic geothermal system. Unlike previous one-way coupled frameworks, our approach implements a closed-loop feedback, where stress redistribution from dynamically simulated seismic events is fed back into the quasi-static THM reservoir model. A 3D thermo-hydro-mechanical model tracks stress build-up during injection until a failure criterion is met, triggering a transition to a dynamic rupture solver that computes spontaneous 3D rupture propagation and seismic wave radiation. An automated coupling protocol ensures seamless data exchange between solvers. We demonstrate the framework by simulating two injection-induced events on a single-fault reservoir model. Results show that event-driven fault displacements and dynamic stress transfers significantly alter reservoir stress states. Simulated Coulomb stress changes, focal mechanisms, and slip distributions align with the ambient stress field and fault geometry. This closed-loop approach provides a robust tool for assessing seismic risk and optimizing injection strategies in geothermal environments.

Highlights

- We present a new modelling approach that links slow fluid-related changes in the subsurface with rapid fault movement.
- The method follows how a fault becomes unstable, from gradual stress changes to sudden slip and shaking.
- The two simulators interact automatically, allowing the subsurface and the fault to influence each other in real time.
- The results show how fluid injection affects fault slip, helping improve safety in geothermal projects.

Keywords Induced seismicity · Geothermal reservoirs · Fault reactivation · Coupled modeling · Dynamic rupture

✉ Rahim Habibi
Rahim.habibi@kit.edu

[1] Institute of Applied Geosciences, Karlsruhe Institute of Technology (KIT), Adenauerring 20b, 76131 Karlsruhe, Germany

[2] Department of Earth and Environmental Sciences, Ludwig Maximilian University of Munich, Munich, Germany

[3] Institute of Geophysics and Planetary Physics, Scripps Institution of Oceanography, University of California San Diego, La Jolla, CA, USA

1 Introduction

Although geothermal energy can play a role to meet the targets of the 2030 Agenda for Sustainable Development ("www.unosd.un.org," 2015) and provide accessible, reliable, and sustainable energy worldwide, its utilization faces challenges. In particular, the possible environmental and social impacts slow down the development of the associated systems (de Jesus 2016), specifically, the risk of induced seismicity, especially in continental Europe (Kohl and Mégel 2007).

Published online: 21 July 2026

Induced seismicity, defined as earthquakes caused by human activities, occurs in various contexts, such as geothermal energy production, mining, waste-water underground disposal, or hydrocarbon extraction (McGarr et al. 2002). Among these, fluid injection has emerged as a significant contributor, especially in the context of subsurface reservoir exploration and development (Foulger et al. 2018). In this study, we distinguish between 'induced' and 'triggered' seismicity: the term 'induced' refers to events primarily driven by pore-pressure and thermoelastic stress changes associated with operations, whereas 'triggered' refers to events in which injection-related stress perturbations advance the timing of failure on faults already close to rupture.

Deep geothermal reservoirs are generally fractured and faulted media, whose degree of fracturing can vary depending on the reservoir type. In enhanced geothermal systems (EGS), the rock matrix is almost impermeable but stimulation of the fracture and fault network near the wells aim to ease and improve fluid circulation. On the contrary, hydrothermal systems exhibit high matrix permeability. In both settings, however, the forced fluid flow injection and circulation can induce and trigger seismic events on fractures and faults (Beeler 2004; Gaucher et al. 2015). Hence, several EGS projects had to be abandoned following the occurrence of induced seismicity during their stimulation phases. For instance, on 8 December 2006, hydraulic stimulation at the Basel (Switzerland) geothermal site triggered an M_L 3.4 event at a depth of about 4.6 km that led to numerous damage claims and eventually cancelation of the project (Kraft and Deichmann 2014). On 15 November 2017, the M_L 5.4 earthquake in Pohang (Korea) was triggered by hydraulic stimulations at similar depths and remains the most destructive earthquake ever recorded in the country, causing substantial damage to infrastructure (Kim et al. 2020). In Vendenheim (France), three events larger than M_{Lv} 3.0 and many other felt events occurred during the deep geothermal field development between 2019 and 2020 (Schmittbuhl et al. 2021).

Many mechanisms leading to fault reactivation have been identified, including direct pore pressure and poroelastic effects (Atkinson et al. 2020), temperature decrease, net fluid volume change, chemical alteration of fracture surface (Majer et al. 2007), or stress transfer and interaction with nearby earthquakes (Moein et al. 2023). All these mechanisms ultimately induce effective stress changes on the fault, promoting failure.

Following these observations, numerous modeling efforts have focused on simulating induced seismicity in geothermal reservoirs, with the aim of forecasting events and evaluating potential ground motion at the surface (Gaucher et al. 2015). The approaches can be grouped into three categories: statistical, physics-based, and hybrid, the latter combining elements of the first two. Each method should deliver, at least, a synthetic catalog of forecasted earthquakes in response to the geothermal operations, i.e., origin time, location, and magnitude, and where possible, the associated surface ground motion. Each method has its strengths and limitations, and the appropriate approach depends on the application, data availability, and the characteristics of the seismic event being forecasted.

Physics-based approaches explicitly account for the physical processes that are assumed to be involved during fluid injection or extraction, how these alter the subsurface conditions and potentially induce earthquakes. They solve numerically coupled equations for fluid flow, heat transfer, and mechanical deformation, allowing to simulate complex interactions in geothermal systems. These approaches are computationally intensive and need observations for calibrating the simulations. However, they give the possibility to link specific geothermal development or exploitation operations with the expected induced seismicity, thus providing a mean to mitigate induced seismicity by optimizing operational strategies.

Physics-based methods for modeling induced seismicity typically use hydro-mechanical (HM) modeling, which couples fluid flow with mechanical deformation to capture how pore-pressure variations affect stress changes. In temperature-sensitive geothermal reservoirs, thermal effects can also play a critical role, motivating thermo-hydro-mechanical (THM) modeling, which extends HM approaches by incorporating thermal processes to simulate temperature-induced stresses and their influence on fault stability.

In most cases, physics-based geomechanical models assume quasi-static conditions and monitor a fault failure criterion, which, if exceeded, suggests fault instability or criticality and may result in a seismic event, but they do not model explicitly the dynamics of the induced earthquake rupture. While the Mohr–Coulomb criterion is the most commonly failure criterion used to evaluate triggering potential (Ge and Saar 2022), other criterion exists and are further discussed in Section 2.1.2.

Dynamic rupture modeling focuses on the physics of the earthquake fault rupture, including its nucleation, propagation and arrest, and its interaction with the seismic wave field, by solving the equations of motion coupled with a friction law (e.g., linear slip-weakening or rate-and-state friction). Galis et al., (2017) introduced a simple framework that combines fracture mechanics and 3D dynamic rupture simulations to model how fluid-induced stress perturbations can trigger earthquakes that either arrest spontaneously or propagate as runaway ruptures. Their work highlights that induced earthquakes can grow well beyond the pressurized zone if sufficient elastic energy is available in the surrounding fault, offering an explanation for observed magnitude scaling with injected volume. Recently, Mosconi et al., (2025) used high-resolution 3D dynamic rupture simulations to explore how modest variations in fault strength and dynamic stress drop, resulting from fluid injection, can determine whether rupture remains confined or grows into a fault-spanning event. These studies emphasize that the transition between self-arresting and runaway ruptures is governed not only by injection parameters but also by the pre-existing stress state, fault frictional properties, and the energy budget of rupture (e.g., Viesca (2016); Viesca and Garagash, (2015)). Incorporating such dynamic effects simulating rupture propagation and ground motion from prescribed initial stress conditions into either HM or THM modeling frameworks is crucial for advancing physics-based approaches to induced seismicity forecasting, supporting improved reservoir monitoring and adaptive traffic-light systems for seismic hazard mitigation. Dynamic rupture models capture processes on short time scales (sub-second for induced seismicity), whereas stress evolution from fluid injection or extraction occurs over much longer periods. Coupling them with quasi-static HM or THM reservoir models allows bridging these time scales.

Different approaches have been proposed to couple quasi-static and dynamic processes relevant to induced seismicity, aiming to capture both the loading process leading to the onset of seismicity and the fault behavior during and after reactivation, and may incorporate modeling interactions between wave propagation, mechanical deformation, fluid flow, and thermal effects. For example, Baisch and Vörös (2010) developed a numerical model to simulate the hydro-mechanical behavior of a reactivated fault at the Soultz-sous-Forêts (France) enhanced geothermal site, during and after seismic events induced by hydraulic stimulation. Once an individual fault element reaches fracture criticality, their approach applies a constant stress drop to the fault element and iteratively redistributes stress around the failing element(s) until a new equilibrium is reached. While their approach does not account for seismic wave mediating rupture propagation, it reasonably captured the observed seismicity pattern at the site, it is applicable to relatively simple fault configurations, and it is computationally efficient. Meng (2017) developed a 3D framework integrating poroelastic flow, viscoelastic relaxation, and frictional fault slip to simulate both static and dynamic crustal deformation, though its applicability to geothermal systems is currently limited by the absence of thermal effects. Jin and Zoback (2018) proposed a 2D model for fluid-induced seismicity that captures pore-pressure changes and fully dynamic spontaneous rupture including poroelastic effects, which also lacks thermal coupling and post-rupture stress evolution. Similarly, Han et al. (2021) presented a poroelastic reservoir-seismicity model, demonstrating predictive capabilities for induced events, yet without incorporating thermoelastic effects. Paap et al. (2020) introduced a three-stage workflow involving geomechanical simulation of a depleting gas field, dynamic rupture modeling**,** and seismic wave propagation modeling, by coupling FLAC and SPECFEM codes in 2D. In their workflow, each numerical code operates on separate grid types and requires interpolation and re-meshing, which can smooth out critical features such as stress concentrations. They limit their study to one seismic event. More recently, Walker et al. (2023) introduced fully coupled continuum poromechanics onto the multiphysics open-source tool PyLith, allowing poroelastic material rheology to be used alongside quasi-static and dynamic modeling of earthquake. Unfortunately, PyLith does not support yet injection or production operations relevant to geothermal systems. Blanco-Martín et al. (2022) coupled TOUGH (Pruess et al. 1999) with Pylith (Aagaard et al. 2013) simulators for modeling THM-fault reactivation in NER300 ULCOS CO2 storage project during injection. The simulation of the model was performed up to the reactivation state and the slip response and the change of stress at different depths of the model were investigated.

A key challenge in coupling a geomechanical quasi-static solver with a dynamic rupture solver is accurately detecting the moment of fault reactivation, which determines when to switch solvers. In several of the frameworks discussed above, this transition is triggered by monitoring the overstress area relative to a theoretical estimate of the critical nucleation size, marking the switch between quasi-static and dynamic time scales. More reliable approaches require the geomechanical solver to incorporate quasi-static faulting, allowing it to capture the gradual progression of slip until slip rate approaches seismic values. For example, Han et al. (2023) proposed a method for controlling and adapting the time steps in hydro-mechanical reservoir models. Their approach automatically refines temporal resolution to accurately capture the quasi-steady progression of slip until it reaches an unstable state, and the subsequent spontaneous rupture propagation. Such integrated approaches, combining quasi-static and dynamic modeling, are considered the most promising way forward for accurately simulating fault behavior.

Several physics-based numerical software and open-source tools have been developed to simulate induced seismicity (Appendix A), each designed with specific features tailored to different applications. Beyond financial and ergonomic aspects, the choice of the appropriate tool depends on factors, such as the field of application, the scale and geological context of the case study, the coupled processes to be taken into account, and the temporal extent over which induced seismicity is modeled. With respect to this last aspect, tools differ in their capabilities to model key processes related to induced seismicity: injection operations to fault failure (FF) dynamic rupture propagation (RP) and feedback effects (FB) between injection operations and seismic events, enabling the simulation of multiple-event sequences. Existing methods often rely on one-way coupling or simplified stress-update schemes, limiting their ability to capture the feedback between the induced seismic event and reservoir evolution. Simplified stress updates, often quasi-static, may fail to capture the evolution and final slip distribution of the dynamic events, and may not capture fine-scale local stress concentrations. In contrast, our framework implements a closed-loop approach, where stress redistribution from dynamically simulated seismic events feeds back into the quasi-static THM model, allowing high-resolution, feedback-driven simulations of induced seismicity. The review indicates that no existing software can fully simulate fluid injection or extraction in geothermal reservoirs while modeling the rupture dynamics of multiple induced seismic events and their feedback on geothermal reservoir properties and stress state. To fill this gap, we propose a framework that couples 3D THM modeling and 3D dynamic rupture modeling, offering a comprehensive approach for better understanding and analyzing induced seismicity in faulted geothermal systems. To model the behavior prior to and after the onset of induced seismicity, we use TIGER, a MOOSE-based open-source application (see Section 2.1) allowing us to simulate THM and solute transport in 3D faulted-geothermal reservoirs (Gholami Korzani et al. 2020). TIGER offers high spatial resolution for simulating long-term THM processes in fractured reservoirs, making it well suited for capturing the quasi-static evolution of stress and pore pressure over the lifetime of a geothermal reservoir exploitation. To simulate the dynamics of induced earthquakes, modeled as dynamically propagating shear ruptures on predefined frictional interfaces, controlled by a friction law and their associated stress changes, we use SeisSol (Dumbser and Käser 2006; Pelties et al. 2014; Uphoff et al. 2024). SeisSol is a high-performance dynamic rupture code capable of resolving seismic wave propagation and rupture processes with high temporal and spatial resolution, down to milliseconds and centimeters, respectively. The complementary nature of these tools and their high degree of optimization and maturity makes their coupling particularly powerful for fully capturing the complex spectrum of induced seismicity, from injection operations to dynamic rupture.

In Section 2, we describe the physical components and governing equations used to capture the THM processes in the geothermal reservoir during injection operations, assess fault criticality, and simulate seismic rupture and wave propagation. The numerical implementations in the TIGER and SeisSol software packages, as well as the framework developed to couple them, are also detailed. Section 3 introduces the synthetic model designed to validate the coupling scheme, with results presented in Section 4. Following the discussion in Section 5, we draw conclusions and propose perspectives for future work.

2 Methods

We use a compound numerical approach to simulate the thermo-hydro-mechanical response of the geothermal system to the fluid circulation, to assess possible failure on faults and, if relevant, propagate the seismic rupture on the fault. The approach couples two open-source applications, one dedicated to the reservoir simulation, TIGER, and the other to the dynamic propagation of seismic rupture, SeisSol. Both codes are detailed in the following as well as their coupling.

2.1 Governing Equations

2.1.1 Thermo-hydro-mechanical Model

A finite-element in-house open-source application called TIGER (THMC sImulator for GEoscientific Research), introduced by (Gholami Korzani et al. 2020), is utilized to simulate the thermo-hydro-mechanical behavior of the geothermal system. The application is based on the object-oriented framework MOOSE (Multiphysics Object-Oriented Simulation Environment) (Permann et al. 2020) and can simulate thermal, hydraulic, and mechanical behavior as well as solute transport in porous and faulted geothermal reservoirs, in a fully coupled manner.

In TIGER, the hydraulics is satisfied by the mass transport equation, which accounts for missing dimensions in lower-dimensional elements such as fractures (2D) and wells (1D) through the scale factor b, as found in other publications such as GOLEM (Cacace and Jacquey 2017) or OpenGeoSys (Watanabe et al. 2012)

$$bS\frac{\partial P}{\partial t} + b\alpha\frac{\partial \varepsilon_{vol}}{\partial t} + \nabla \cdot (b\boldsymbol{q}) = Q \tag{1}$$

$$\boldsymbol{q} = \frac{k}{\mu_f}\left(-\nabla P + \rho^f \boldsymbol{g}\right), \tag{2}$$

where S is the constrained specific storage of the porous media (Pa^{-1}), P is the pore pressure (Pa), t is the time (s), α is the Biot coefficient, ε_{vol} is volumetric strain of porous medium, Q is the source term for injection/production (kg/s), $\boldsymbol{q}$ is the fluid or Darcy velocity vector (m/s), $\boldsymbol{k}$ is the permeability tensor (m^2), μ_f is the brine dynamic viscosity (Pa·s) combined with permeability known as the mobility term, ρ^f is the fluid density (kg/m^3), and $\boldsymbol{g}$ is the gravitational acceleration vector (m/s^2). The scale factor b plays a crucial role in accurately representing the physical characteristics of lower-dimension mesh elements embedded in higher-dimension mesh elements. For example, for elements like wells or pipes, the scale factor represents the cross-sectional area, ensuring that flow rates and other related properties are accurately modeled. For fractures or faults, the scale factor represents the (hydraulic) aperture of the fracture, which influences permeability and fluid flow within the simulation.

The permeability depends on porosity according to Eq. 3 where the current permeability in the model is proportional to the initial permeability value ($\boldsymbol{k}_0$) and the ratio of the current (ϕ) over the initial porosity (ϕ_0) at the power of m, m is a material constant ranging from 3 to 5 for rocks

$$\boldsymbol{k}(\phi) = \boldsymbol{k}_0 \left(\frac{\phi}{\phi_0} \right)^m. \tag{3}$$

The thermal response is modeled using the heat transfer equation solved for temperature which can be mathematically estimated via the advection-diffusion equation in which the advective term is implemented in non-conservative form, which is appropriate for advection-dominated geothermal systems where $\nabla \cdot (b\boldsymbol{q})$ contributions to thermal energy are secondary

$$b(\rho c_p)_{eff} \frac{\partial T}{\partial t} - \left(\nabla \cdot \left(b\lambda_{eff} \cdot \nabla T \right) + \rho^f c_p^f b\boldsymbol{q} \cdot \nabla T \right) = bQ, \tag{4}$$

where ρ is the effective density of the porous media (kg/m^3), c_p is the effective specific heat capacity of the porous media (J·kg^{-1}·K^{-1}), T is the temperature (K), t is the time (s), λ_{eff} is the effective heat conductivity tensor of the porous media (kg·m·s^{-3}·K^{-1}), ρ^f is the density of the fluid (kg/m^3), c_p^f is the specific heat capacity of the fluid (J·kg^{-1}·K^{-1}), and $\boldsymbol{q}$ is the Darcy velocity in the porous media (m/s), the same as in Eq. 2 and Q (W/m^3) represents heat source. In Equation 4, $(\rho c_p)_{eff}$ represents the effective volumetric heat capacity of the saturated porous medium, calculated as the volume-weighted average of the phase products: $(\rho c_p)_{eff} = \phi \rho^f c_p^f + (1-\phi)\rho^s c_p^s$, where ϕ is the porosity, ρ^s is the density of the solid (kg/m^3), and c_p^s is the specific heat capacity of the solid (J·kg^{-1}·K^{-1}). Following the numerical implementation in TIGER, all terms in the energy balance are multiplied by the scaling factor, ensuring consistent heat transport integration across different mesh dimensions.

To estimate the deformation and stress, TIGER calls the Tensor Mechanics Module from MOOSE (INL 2023). The governing equation is the momentum balance equation (Jaeger et al. 2007). The coupling of hydraulic and solid mechanics (poroelasticity) is written in effective stress form as follows:

$$\nabla \cdot \boldsymbol{\sigma}' + \rho_s \boldsymbol{g} = 0 where \boldsymbol{\sigma}' = -\boldsymbol{\alpha P}\mathbb{I}, \tag{5}$$

with σ is the total stress tensor, $\boldsymbol{\sigma}'$ the effective stress tensor, α the Biot coefficient, and ρ_s the solid rock density. We follow the sign convention for rock mechanics where the compression is negative for stress. Similarly, thermal–mechanical coupling is modeled through linear thermoelasticity Eq. 6, where stress is related to strain via the fourth-order isotropic elasticity tensor, C according to Hook's law given in Eq. 8

$$\Delta \boldsymbol{\sigma_{ij}} = \boldsymbol{C_{ijkl}}(\Delta \boldsymbol{\varepsilon_{kl}} - a_f \Delta T \delta_{ij}) \tag{6}$$

$$\Delta \boldsymbol{\varepsilon_{ij}} = \frac{1}{2}\left(\frac{\partial \Delta u_i}{\partial x_j} + \frac{\partial \Delta u_j}{\partial x_i}\right) \tag{7}$$

$$\boldsymbol{C}_{ijkl} = \lambda \delta_{ij}\delta_{kl} + 2\mu(\delta_{ik}\delta_{jl} + \delta_{il}\delta_{jk}); \tag{8}$$

$\Delta\boldsymbol{\sigma}'$ is the change of effective stress in time, $\boldsymbol{C}$ is the elasticity tensor, $\Delta\boldsymbol{\varepsilon}$ is the strain change in time, α_f is the volumetric drained thermal expansion coefficient, ΔT is the temperature change, δ is the Kronecker delta, λ is the shear modulus or first Lamé parameter, and μ is the second Lamé parameter.

TIGER solves the equations for pressure (fluid flow), temperature (heat transfer), and displacement (solid mechanics) as main variables, but stress calculation can be carried out as a by-product of simulation from the framework viewpoint. As in the hydraulic equations, the porosity is hidden in the solid mechanics equations. Considering a fully saturated, single-phase, single-component fluid, the porosity is connected to the volumetric strain change ($\Delta\varepsilon_v$) and fluid density (ρ) through the mass continuity equation for the fluid in the porous medium

$$\frac{\delta}{\delta t}(\phi\rho) = -\phi\rho\Delta\varepsilon_v. \tag{9}$$

This form assumes incompressible solid grains ($\alpha = 1$), consistent with the Biot coefficient adopted throughout this study. Under this assumption, porosity changes are driven solely by skeleton volumetric strain, as derived from the general poromechanical framework of (Coussy 2004). This simplification is physically justified for fault damage zones where fracture compliance dominates matrix compressibility, and it ensures robust numerical coupling during rapid pressure evolution. Since fluid density depends on the temperature and pressure changes (ΔT and ΔP, respectively), the left-hand side of the equation can be written as Eq.10 with M, α, and A being Biot Modulus, Biot coefficient, and effective volumetric thermal expansion coefficient. Furthermore, the Biot modulus and the effective volumetric thermal expansion can be calculated by Eqs. 11 and 12, where K_f and K refer to the solid and fluid bulk modulus, respectively, and α_T and α_f are the thermal expansion coefficient of the drained porous skeleton and volumetric thermal expansion coefficient, respectively (INL 2023)

$$\frac{\partial}{\partial t}(\phi\rho) = \rho\left(\frac{1}{M}\frac{\partial P}{\partial t} + \alpha\frac{\partial \varepsilon_{vol}}{\partial t} - A\frac{\partial T}{\partial t}\right) \tag{10}$$

$$\frac{1}{M} = \frac{\phi}{K_f} + \frac{(1-\alpha)(\alpha-\phi)}{K} \tag{11}$$

$$A = (\alpha - \phi)\alpha_T + \phi\alpha_f. \quad (12)$$

TIGER was validated against thermal, hydraulic processes but also against coupled hydro-thermal processes (Gholami Korzani et al. 2020) or hydro-solute processes (Egert et al. 2021). To verify the hydro-mechanical coupling (poroelasticity), validation was made for the case proposed by (Altmann et al. 2010), which is based on the analytical solution of (Rudnicki 1986; Egert 2022). TIGER has been applied to simulate various problems in geothermal systems, including fluid flow in fractures (Egert et al. 2021), heat storage (Stricker et al. 2024), and transport in fractured EGS reservoirs (Yan et al. 2022).

2.2 Stress Implementation on Fault and Failure Criterion

To simulate potential seismic activity in a porous and faulted geothermal reservoir using TIGER, it is necessary to incorporate a failure criterion on the faults within the modeled domain. The Mohr–Coulomb (MC) failure criterion is well suited for systems with pre-existing weak planes embedded in a porous matrix, as it evaluates the stress state to determine when shear failure occurs along these planes, in contrast to alternative criteria such as Drucker–Prager and von-Mises, which are primarily designed to capture yielding within the bulk rather than shear failure (Vermeer 1998), while cap models (e.g., CamClay) are developed for plastic compaction of porous media and capture deformation rather than frictional slip, and the Hoek–Brown criterion is empirical, intended for rock mass failure modeling but is not friction-based (Muir Wood 1990; Vermeer 1998; Eberhardt 2012). Furthermore, the MC can directly integrate pore-pressure effects, reducing fault effective normal stress, making it particularly appropriate for simulating fault reactivation due to fluid injection.

Formulating the MC failure criterion requires computing normal and shear stresses on the fault, obtained by projecting the stress tensor onto the fault plane. The stress traction, $\boldsymbol{T^n}$, acting on a plane of normal $\mathbf{n}$ and crossing an arbitrary point inside a rigid body can be calculated as follows:

$$\boldsymbol{T^n} = \boldsymbol{\sigma}' \cdot \boldsymbol{n}, \quad (13)$$

where $\boldsymbol{\sigma}'$ is the stress tensor and $\boldsymbol{n}$ is the unit normal vector to the considered plane. The traction can be decomposed in two components: one perpendicular to the plane, the effective normal stress $\sigma_n\prime$ (which is a scalar), and one orthogonal to it, the shear stress τ_n vector

$$\sigma_n\prime = \boldsymbol{T^n} \cdot \boldsymbol{n} = \boldsymbol{n} \cdot .\boldsymbol{\sigma}' \cdot \boldsymbol{n} \quad (14)$$

$$\begin{aligned} \tau_n &= T^n - \sigma_n' n = \sigma' n - \left(n \cdot \sigma' \cdot n\right) n \\ \tau_n^2 &= (T^n)^2 - \sigma_n^2. \end{aligned} \quad (15)$$

The local fault traction vector has generally a strong influence on the direction of displacement during failure (rake angle) and, therefore, on the focal mechanism of the seismic event.

In the proposed workflow, the Coulomb stress change is monitored to detect the MC failure. The Coulomb stress change, ΔCFS, is defined as (Kivi et al. 2022)

$$\Delta CFS = \Delta\tau - \mu|(\Delta\sigma + \Delta P)|. \quad (16)$$

When ΔCFS is positive, the system is stable, but when it is negative, the failure criterion is reached. The sign of ΔCFS can be evaluated at the scale of a single element of the mesh or over a larger area.

We intentionally use an element-local failure criterion that neglects the energy balance considerations required to sustain dynamic rupture, which is sufficient to demonstrate code coupling. A consequence of such a local failure criterion is that rupture evolution remain quasi-static within the dynamic rupture models. In fact, while the failure of a single-fault element may produce local stress drops and transient slip, the elastic stiffness of the surrounding medium typically prevents further rupture growth.

Dynamic propagation can occur only when rupture initiates over a sufficiently large region that exceeds the critical nucleation size. In this case, the energy release rate at the rupture front equals or exceeds the fracture energy, allowing self-sustained propagation. Several theoretical estimates of the critical nucleation size have been proposed (e.g., Andrews 1976; Uenishi and Rice 2003; Shi and Day 2013)), and their consistency with the numerical implementation of *SeisSol* has been evaluated by (Galis et al. 2017) who derived a general functional expression for the critical nucleation length, partly from numerical simulation with *SeisSol*. It simplifies under near-critical stress conditions to the formulation of (Uenishi 2009)

$$L_c = 0.624 \frac{C(\nu)\mu D_c}{(1-\nu)(\tau_s - \tau_d)}, \quad (17)$$

where μ is the shear modulus, ν is Poisson's ratio, D_c is the characteristic slip-weakening distance, τ_s and τ_d are the static and dynamic fault strengths, and $C(\nu)$ is a dimensionless function of Poisson's ratio. τ_s and τ_d typically depend on the effective normal stress, which depend on local stress and pore pressure.

It should be emphasized that theoretical estimates of L_c are obtained under idealized, homogeneous conditions. In fluid injection scenarios, however, pore pressure and effective stress vary significantly in space and time, making the determination of a reliable nucleation size highly uncertain.

Modeling quasi-static faulting coupled with geomechanical modeling could allow modeling accurately the onset of slip in highly heterogeneous conditions, but would require a numerical challenging higher degree of integration of the earthquake and geomechanical model. We plan to explore more realistic failure criterion and coupling strategies in the future.

2.3 Earthquake Rupture Dynamics

To model induced seismicity and wave propagation in the modeled domain, the open-source software SeisSol (Uphoff et al. 2024; Gabriel et al. 2025) is utilized. SeisSol implements the Arbitrary high-order accurate DERivative Discontinuous Galerkin method (ADER-DG) (Dumbser and Käser 2006) to solve the 3D dynamic rupture problem coupled to seismic wave propagation (e.g., (Harris et al. 2018)). Besides modeling the spatial and temporal evolution of earthquake rupture, SeisSol provides various output products, including the moment magnitude of the event, surface displacements, and the ground shaking caused by the radiated seismic waves. In the SeisSol framework, the fault geometry is represented as a geometrical interface within an unstructured tetrahedral mesh. Pelties et al. (2014) verified SeisSol's capability in simulating complex geometries, e.g., across fault intersections and including heterogeneity of physical model parameters along the fault as well as complicated friction laws such as rate-and-state friction.

Regarding the governing equations, SeisSol solves the elastic (or viscoelastic, poroelastic) seismic wave equation in the velocity-stress formulation where six components of stress and three components of velocity are considered as unknowns in the equation (e.gKrenz et al. 2021a, b; Wolf et al. 2025). The set of the equations is as follows (for an elastic material):

$$
\begin{aligned}
&\frac{\partial}{\partial t} - (\lambda + 2\mu)\frac{\partial}{\partial x}u - \lambda\frac{\partial}{\partial y}v - \lambda\frac{\partial}{\partial z}w = 0,\\
&\frac{\partial}{\partial t}\sigma'_{yy} - \lambda\frac{\partial}{\partial x}u - (\lambda + 2\mu)\frac{\partial}{\partial y}v - \lambda\frac{\partial}{\partial z}w = 0,\\
&\frac{\partial}{\partial t}\sigma'_{zz} - \lambda\frac{\partial}{\partial x}u - \lambda\frac{\partial}{\partial y}v - (\lambda + 2\mu)\frac{\partial}{\partial z}w = 0,\\
&\frac{\partial}{\partial t}\sigma'_{xy} - \mu\left(\frac{\partial}{\partial x}v - \frac{\partial}{\partial y}u\right) = 0,\\
&\frac{\partial}{\partial t}\sigma'_{yz} - \mu\left(\frac{\partial}{\partial z}v - \frac{\partial}{\partial y}w\right) = 0,\\
&\frac{\partial}{\partial t}\sigma'_{xz} - \mu\left(\frac{\partial}{\partial z}u - \frac{\partial}{\partial x}w\right) = 0,\\
&\rho\frac{\partial}{\partial t}u - \frac{\partial}{\partial x}\sigma'_{xx} - \frac{\partial}{\partial y}\sigma'_{xy} - \frac{\partial}{\partial z}\sigma'_{xz} = 0,\\
&\rho\frac{\partial}{\partial t}v - \frac{\partial}{\partial x}\sigma'_{xy} - \frac{\partial}{\partial y}\sigma'_{yy} - \frac{\partial}{\partial z}\sigma'_{yz} = 0,\\
&\rho\frac{\partial}{\partial t}w - \frac{\partial}{\partial x}\sigma'_{xz} - \frac{\partial}{\partial y}\sigma'_{yz} - \frac{\partial}{\partial z}\sigma'_{zz} = 0,
\end{aligned}
\tag{18}
$$

where $\sigma'_{xx}, \sigma'_{yy}, \sigma'_{zz}$, are normal stress components and $\sigma'_{xy}, \sigma'_{yz}, \sigma'_{xz}$ are shear stress components. The velocity components are defined as u, υ, ω in x-, y-, and z-directions respectively, λ and μ refer to the *Lamé constants,* and ρ is the mass density of the medium. In addition, SeisSol supports various friction laws such as linear slip weakening and rate-and-state friction, whose fault strength is to be considered in the framework of the failure criterion. For example, the fault strength in the linear slip-weakening law is defined as follows (Ida 1972):

$$
\tau = \left[\mu_s - (\mu_s - \mu_d)\frac{min(d, D_c)}{D_c}\right].(\sigma'_n), \tag{19}
$$

with τ the shear strength of the fault, μ_s the static friction coefficient, μ_d is the dynamic friction coefficient, d the slip distance, and D_c the critical slip-weakening distance. When slip accumulates, the fault strength drops from static to dynamic shear strength, as defined by the friction law. SeisSol propagates fault slip, which is used to calculate the seismic moment and the moment magnitude. In this workflow, the MC criterion controls fault activation, while the friction law governs slip evolution, both of which are essential inputs for determining earthquake magnitude.

The dynamic rupture is initiated by applying the stress from the THM modeling, which includes an overstressed area, the size of one or more mesh elements, over which the rupture nucleates. As the rupture begins to slip, the motion at the rupture front generates dynamic stress changes in the surrounding fault, increasing shear stress ahead of the rupture front. These neighboring areas of the fault may now experience shear failure, leading to the dynamic propagation of the rupture, advancing into areas newly brought to failure. The rupture eventually stops when It encounters a barrier (e.g., stronger patch, an unfavorable stress condition), or when energy is insufficient to overcome resistance ahead of the front. SeisSol has been applied in various settings for modeling dynamic rupture, seismic activity, and earthquakes.

2.4 Coupling of TIGER and SeisSol

In this section, the proposed coupled workflow is described with emphasizing on the computational domain used and variables transferred by the codes. The exact state at which the MC criterion is reached in the THM simulation is determined via an iterative process (see also discussion in the introduction section), before the output from this state is passed to the dynamic rupture solver. In the following, we detail our workflow step by step. From a numerical computational viewpoint, the time and spatial scale of each mode is different which challenges data exchange.

2.5 Meshing

As mentioned above, both simulators are finite-element codes; TIGER implements a continuous Galerkin method and SeisSol a discontinuous Galerkin method. The challenges of coupling a continuous Galerkin with a discontinuous Galerkin method in our workflow are discussed in the Discussion section. While TIGER can use hexahedral or tetrahedral meshes, SeisSol requires tetrahedral elements (specifically, well-shaped ones are preferred as they impact the time step calculation, although local time-stepping loosens this constraint Breuer et al. 2016; Uphoff et al. 2017) The simplest option is then to use the same tetrahedral mesh for both. Practically, the mesh (computational domain) is here generated with Gmsh (Geuzaine and Remacle 2009). We note that this option may be suboptimal as both codes have different resolution requirements. In fact, mesh size plays a key role in the resolution and accuracy of the numerical solution, and the mesh has to capture the processes modeled in both codes. Specifically, TIGER needs high resolution near the well, and can accommodate coarser resolution elsewhere on faults. Therefore, the mesh is highly refined around the injection point, up to 10cm element length, and the mesh size gradually is increased away from the point. In contrast, SeisSol needs a uniform resolution everywhere on faults, high enough to resolve the process zone width, the characteristic length scale over which fault weakening occurs, and may also require high resolution in the volume if high-frequency synthetics are required, or to properly capture potential seismic waves mediated multi-fault dynamic triggering. Problems posed by differing simulation and output resolution and their consequences on the accuracy of the data transfer are further discussed in Section 5.2.

The adopted element size near the injection point is several orders of magnitude smaller than the characteristic scales of pore-pressure diffusion and stress redistribution along the fault domain. Consequently, the mesh resolution is sufficient to resolve the spatial variations of the key state variables controlling fault reactivation. In quasi-static, injection-driven problems, deformation evolves gradually, and the governing fields (stress and pore pressure) remain smooth in space and time. Unlike dynamic rupture simulations, the slip onset is not sensitive to inertial effects or critical nucleation size, and the numerical resolution is primarily controlled by the ability to capture pressure-induced stress perturbations. The 10 cm refinement adopted here lies well within the range used in comparable THM studies of injection-induced fault reactivation (e.g., Rutqvist et al. (2015)). While a complete mesh convergence analysis is beyond the scope of this study, the combined physical arguments, smoothness of computed fields, and consistency with previously validated THM injection models support the physical robustness of the adopted mesh configuration.

2.6 Failure Timing

TIGER evolves slow processes (e.g., fluid pressure diffusion, thermal expansion), where time steps might be on the order of hours, days, or even longer as the solution progresses steadily, leveraging TIGER's implicit time scheme (e.g., backward Euler or Crank–Nicolson). In contrast, SeisSol models dynamic rupture with high-frequency wave propagation using an efficient explicit time scheme (ADER-DG), requiring time steps in microseconds to maintain numerical stability (CFL condition). For example, after 5 years of injection, the failure criterion is satisfied in TIGER, at which point the THM simulation is stopped. A dynamic rupture simulation of the induced earthquake is then carried out using SeisSol, until rupture arrest occurs and the seismic waves have exited the computational domain, typically within a few tens of seconds. The difference in the time scale of the modeled processes allow for the two codes to be sequentially coupled.

To converge toward the critical state, the exact state at which the fault is about to reactivate, we apply an iterative strategy, halving the time step size until the critical state is reached. Table 1 illustrates the algorithm, using arbitrary values, more details in the following. The simulation begins with a prescribed initial time step, which then gradually increases, in this example approaching a larger near-constant time step size (e.g., 1 month). After a couple of time steps, the failure criterion is exceeded, indicating that the large time steps has advanced the system beyond the critical state, which is somewhere between the last time step and the current time step. Table 1 illustrates of such a situation, in which, at the end of the 4^{th} time step, the MC criterion is exceeded, implying that the critical state, at which the failure value reaches 1, is between the 3^{rd} and 4^{th} time steps. The model is re-started from the previous time step with a time step size reduced by half. In the second try for the 4^{th} time step, the failure value is larger than 1 again, prompting TIGER to try an even smaller time step (one-fourth of the initial time step). The iterative process stops when the time step size falls below a given threshold (e.g., 1 s), at which point the THM simulation is terminated. From this state, the dynamic rupture model (SeisSol) is initialized using the last stress state of TIGER.

2.7 Automating the Workflow

The connection point between TIGER and SeisSol can span multiple events sequentially. After each earthquake, the stress change induced by the dynamic rupture is added to the stress state of the TIGER model, which is then reinitiated and advanced until the next critical state is reached. This multi-event workflow is illustrated in Fig. 1. In this

Table 1 Detection of reactivation moment using arbitrary values

Solving try	Time step	Start time in solution time	Dt (time step size, s)	End time in solution time	Failure value	Solution status
1	1	0	0.3	0.3	0.3	Accepted
2	2	0.3	0.3	0.6	0.6	Accepted
3	3	0.6	0.3	0.9	0.9	Accepted
4	4	0.9	0.3	1.2	1.2	Aborted
5	4	0.9	0.15	1.05	1.05	Aborted
6	4	0.9	0.075	0.975	0.975	Accepted
7	5	0.975	0.15	1.125	1.125	Aborted
8	5	0.975	0.075	1.05	1.05	Aborted
9	5	0.975	0.0375	1.0125	1.0125	Aborted
10	5	0.975	0.01875	0.99375	0.99375	Accepted
11	6	0.99375	0.0375	1.03125	1.03125	Aborted
12	6	0.99375	0.01875	1.0125	1.0125	Aborted
13	6	0.99375	0.009375	1.003125	1.003125	Aborted
14	6	0.99375	0.00496875	0.99871871	0.99871871	Accepted

process, the SeisSol simulation time is neglected, as the rupture is assumed to occur instantaneously compared to the much slower THM processes. This assumption is reasonable for induced seismic events in geothermal fields, which typically last only a few seconds. In the proposed workflow, the stress tensor serves as the coupling interface: when TIGER meets the failure criterion, its final stress state is passed to SeisSol. SeisSol then returns the earthquake-induced stress change, which is added to TIGER's stress field before the simulation continues. Practically, TIGER produces an Exodus file, while SeisSol preferentially reads inputs on rectilinear grid stored as Netcdf file, meaning that an interpolation and a format conversion must be performed from exodus to Netcdf. Similarly, the h5 SeisSol output of SeisSol must be converted to Exodus format to be able to add it to the THM stress state. These conversions are done through Python scripts. Thus, each event loop consists of one TIGER simulation, one SeisSol simulation, and two file conversions, including possible interpolation and regridding, which is automated through a shell script (Fig. 1).

3 Synthetic Case Study

3.1 Model Geometry

To illustrate the processing workflow, a synthetic case study of fluid injection into a vertical fault embedded in a reservoir is developed. Such a conceptual model could represent a

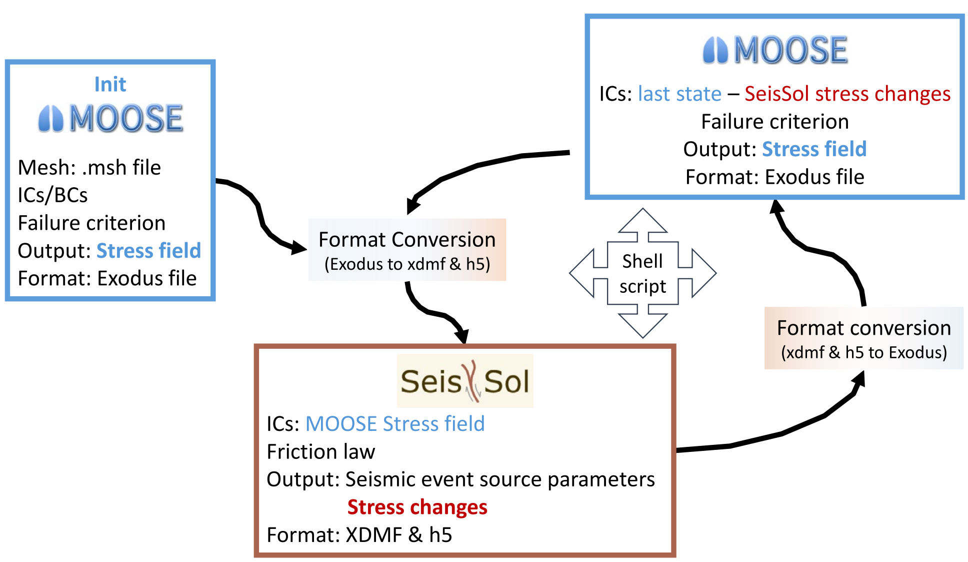

Fig. 1 Schematic representation of the coupling workflow

hydraulic stimulation operation for an EGS or the re-injection of geothermal fluid in a fault.

The model domain is an $8 \times 8 \times 6$ km^3 volume in the x (North), y (East), and z (Depth) directions. A cubic reservoir of 2 km side length, oriented N45°, hereafter referred to as the matrix, is laterally centered in the domain, and reaches the surface. It is crossed in its center by a vertical fault that also strikes N45°. The fault is 2 km long and extends 1.8 km in depth. A 1 cm fault thickness is assumed and is accounted for in TIGER through upscaling (Stricker et al. 2024). A point-source injection is assumed at 1 km depth, located at the center of the fault. All model components are hierarchically embedded, from the smallest feature (injection point) to the largest (the entire domain). Figure 2a shows a top view and a perspective view of the model, while Fig. 2b provides a close-up around the fault. The virtual vertical line ABC passes through the injection point, the fault, the reservoir, and the matrix. Points A and B refer to the points on the fault at surface and at the endpoint of the fault over depth, and point C refers to the bottom of the model. In the following, many of the results will be plotted along this line.

The finite-element mesh is created in Gmsh, where the injection point and the fault are defined as a point (0D) and a 2D triangular surface, respectively, and the reservoir and matrix parts are represented as 3D tetrahedrons. As mentioned above, the same mesh is used in the THM and dynamic rupture models, with the exception of the definition of the boundary elements and the presence of the injection point in the THM model. The generated mesh contains 85881 nodes and 551543 elements. The mesh size ranges from 0.1 m around the injection point to 200 m at the boundaries of the model. The highly refined mesh around the injection point enables accurate representation of the injection operations.

3.2 Material Properties and Boundary Conditions

The vertical component of the lithostatic stress is defined by the gravitational load of the overlying layer. Intentionally, a strike-slip stress regime ($\sigma_{xx} > \sigma_{zz} > \sigma_{yy}$) is defined in the model, so the vertical stress acts as the intermediate principal stress. The other components of the lithostatic stress, i.e., the maximum ($\sigma_{xx} = 1.2\sigma_{zz}$) and minimum ($\sigma_{xx} = 1.2\sigma_{zz}$) principal stresses, are oriented along the x- and y-directions, respectively Hence, the fault is intentionally oriented close to a critical state, allowing it to be reactivated within a short period of time. As shown by (Jaeger et al. 2007), the most critical state for fault reactivation is 45°+ϕ/2 (where ϕ is friction angle). The fault therefore deviates by 15° from this optimal orientation. In the THM model, the side boundaries are fixed only in their normal direction, while the bottom is fixed in all directions, and the top (ground level) is free to move, and the fault is a thin region (modeled as a surface) with enhanced permeability, porosity, and thermal conductivity, and decreased specific heat capacity. We apply Dirichlet conditions for both pore pressure (hydrostatic) and temperature (geothermal gradient) at the top and bottom boundaries. The lateral faces are treated as closed to fluid and heat flow (no-flux Neumann conditions), representing a typical symmetry or far-field assumption in modeling. In SeisSol, the external surfaces are tagged as absorbing and free-surface boundaries in the dynamic rupture model, and the fault as a dynamic rupture interface. Table 2 summarizes the list of boundary conditions applied in the model in both regimes.

The material properties of the fault, reservoir, and matrix including thermal, hydraulic, and mechanical properties are given in Table 3. Some of these properties in the quasi-static regime are representative of the Pullach site (Gaucher and Egert 2022); however, others such as permeability and frictional parameters in the dynamic regime are chosen for numerical stability. While certain material parameters (for example, fault permeability $k = 2 \cdot 10^{-10}$; static friction coefficient $\mu = 0.6$) were selected partly to ensure numerical stability, they remain within physically realistic bounds informed by field data. The permeability value represents an upscaled bulk property for a stimulated fault damage zone, consistent with the upper range of estimates from the Soultz-sous-Forêts EGS site (~10^{-14} m^2 for natural conditions; higher values plausible post-stimulation) (Auradou et al. 2005; Kosack et al. 2010; Zhang et al. 2025). The friction coefficient follows Byerlee's empirical law for crustal rocks ($\mu = 0.6 - 0.86$) and aligns with laboratory measurements on granite gouge under hydro-thermal conditions (Valley and Evans 2007; Lei et al. 2024). Qualitative sensitivity analysis (for example, Pandey and Vishal 2017; Mahmoodpour et al. 2022) indicates that permeability variations of ± 1 order of magnitude primarily affect pressure propagation timescales, while friction coefficient variations mainly influence fault slip thresholds. Coupled permeability-stress feedback may amplify these effects, suggesting that future work should incorporate dynamic property evolution. Because this study focuses on the coupling framework using a realistic but rather idealized geothermal system, and not a specific site, we use a relatively generic set of parameters in our modeling. A systematic sensitivity analysis of the impact of modeling parameters on induced seismicity could be explored in future work, e.g., when investigating a real site.

In the quasi-static THM model, the injection is prescribed as a point-source boundary condition for the thermal and hydraulic components, with a constant flow rate of 20 L/s and a constant injection temperature of 303.15°K.

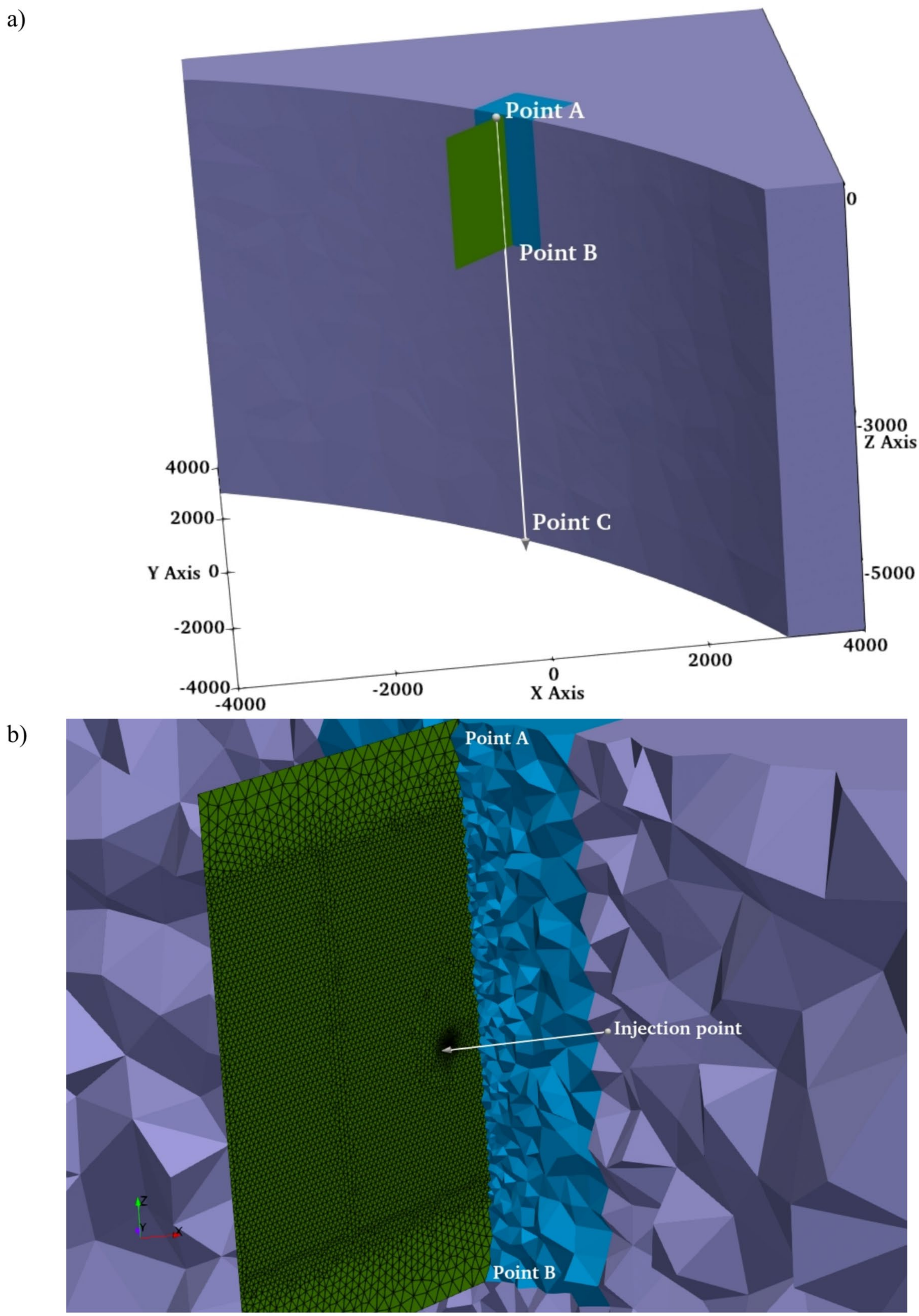

Fig. 2 The geometry of the model including fault, reservoir, and the matrix are shown in green, blue, and purple, respectively; **a** whole domain and **b** zoomed-in view

Table 2 Boundary conditions (BC) applied in the model

Face	Mechanical BC (quasi-static and dynamic)	Hydraulic BC (quasi-static)	Thermal BC (quasi-static)
Top	Free Surface (Neumann $\sigma.n = 0$)	Dirichlet (fixed pressure)	Dirichlet (fixed temperature)
Bottom	Fixed ($u_x = u_y = u_z = 0$)	Dirichlet (fixed pressure)	Dirichlet (fixed temperature)
Front/Back	Roller ($u_x = 0$)	No Flow (Neumann)	Insulated (Neumann)
Left/Right	Roller ($u_y = 0$)	No Flow (Neumann)	Insulated (Neumann)

Table 3 Thermo-hydro-mechanical properties of the model used in the quasi-static THM and dynamic rupture models

Parameter	Description	Value and unit
THM model		
Porosity	Reservoir and matrix	5%
	Fault	15%
Permeability	Matrix	3e-18 m^2
	Reservoir	3e-17 m^2
	Fault	20e-11 m^2
Fluid compressibility	Matrix	2.16e+09 m^2/N
Fluid viscosity	Matrix	0.85 mm^2/s
Fluid heat capacity	Matrix	3800 $J \cdot kg^{-1} \cdot K^{-1}$
Fluid thermal conductivity	Matrix	0.6 W/(m.K)
Fluid density	Matrix	1000 kg/m^3
Thermal expansion coefficient	Matrix	1e-6 K^{-1}
Specific heat capacity	Reservoir and matrix	1400 $J \cdot kg^{-1} \cdot K^{-1}$
	Fault	1000 $J \cdot kg^{-1} \cdot K^{-1}$
Thermal conductivity	Reservoir and matrix	2 W/(m.K)
	Fault	3 W/(m.K)
Young's modulus	Reservoir and matrix	15e9 Pa
	Fault	15e9 Pa
Poisson's ratio	Reservoir and matrix	0.2 (-)
	Fault	0.2 (-)
Biot-Willis coefficient	Matrix	1 (-)
Solid bulk modulus	Matrix	8e9 Pa
Rock density	Matrix	2500 kg/m^3
Injection flow rate	Injection point	20 l/s
Injection temperature	Injection point	303.15°K
Dynamic rupture model		
Rock density	Matrix	2500 kg/m^3
Critical slip-weakening distance	Fault	1.5 m
Fault static frictional coefficient	Fault	0.6
Fault dynamic frictional coefficient	Fault	0.2
Young's modulus	Matrix	15e9 Pa
Poisson's ratio	Matrix	0.2 (-)

3.3 Initial Conditions

For the initial conditions of fluid circulation, the pressure is set to hydrostatic over depth and the temperature follows a gradient of 0.03° C/m. In the dynamic rupture model, the initial conditions consist of the stress field, which is initialized using the stress state in the THM model at the reactivation state. Initial velocities are set to zero. As mentioned in Section 2.2.3, after the seismic event, the stress field in TIGER is updated by adding the stress change induced by the seismic event. The THM simulation is then run with this updated stress field until a new static equilibrium is reached, allowing the displacement field to adjust accordingly. The change of stress field from the reactivation moment are used to initialize the new THM model.

4 Multi-event Strategy

In the following, we present the response of the synthetic model to fluid injection into the fault. To illustrate the coupling and interaction between TIGER and SeisSol, we simulate two seismic events. Figure 3 shows the timeline of the simulation with the two induced seismic events (stars) and the different stages of the simulation workflow that will be described and whose results will be given. Hence, the end of stages pre-slip 1 and pre-slip 2 correspond to the critical state of the reservoir when fault reactivation can occur. The seismic event dynamics are simulated in stages slip 1 and slip 2, once the stress state from TIGER is transferred to SeisSol (stages pre-slip 1—slip 1 and pre-slip 2—slip 2). Following each seismic event dynamics simulation, fluid injection resumes in stages post-slip 1 and post-slip 2, once the stress changes from SeisSol have been transferred to TIGER (stages slip 1—post-slip 1 and slip 2—post-slip 2). The key aspects of the induced seismicity modeling are highlighted, in particular the reactivation time, the stress redistribution patterns after rupture, the displacement along and across the fault plane, and the spatial extent of the total slip. Table 4 summarizes the characteristics of the two induced seismic events.

4.1 Pre-slip 1

Once the synthetic model is initialized with the prescribed stress regime, the predefined boundary and initial conditions, it is run to steady state until static equilibrium is reached. During this phase, consolidation takes place resulting in a 15.2 m subsidence at the top of the model. Figure 4a shows the depth profiles of the diagonal components of the stress tensor (pink, green, cyan curves), pore pressure (black curve), and temperature (purple dotted curve) measured along the vertical [AC] segment crossing the center of the model (see Fig. 4) and obtained at static equilibrium. Figure 4b shows the same parameters as well as the normal (red curve) and Coulomb (blue curve) stresses along the [AB] fault segment (see Fig. 2).

Once the static equilibrium has been reached, the 20 l/s injection is initiated. After ~3.3 years of operations (105 552 000 s), the fault reaches a reactivation critical state at point (0, 0, -1000). Figure 5 shows the normal, shear, and Coulomb stress changes at the reactivation time (last time step in TIGER) along the [AB] fault segment. The element-wise output (one value per element) highlights that the MC failure criterion is reached at one element only in this case (the reason of elemental output is discussed in Section 5.1).

4.2 Pre-slip 1—Slip 1

In this section, the accuracy of data transformation from TIGER to SeisSol is verified. As mentioned in Section 2.2, the parameter coupling both software is the stress tensor. At reactivation time, the next step of the workflow consists in projecting and interpolating the stress data generated by TIGER provided element-wise on the unstructured tetrahedral grid of TIGER onto a rectilinear grid readable by SeisSol. We verify that the transfer is performed correctly by

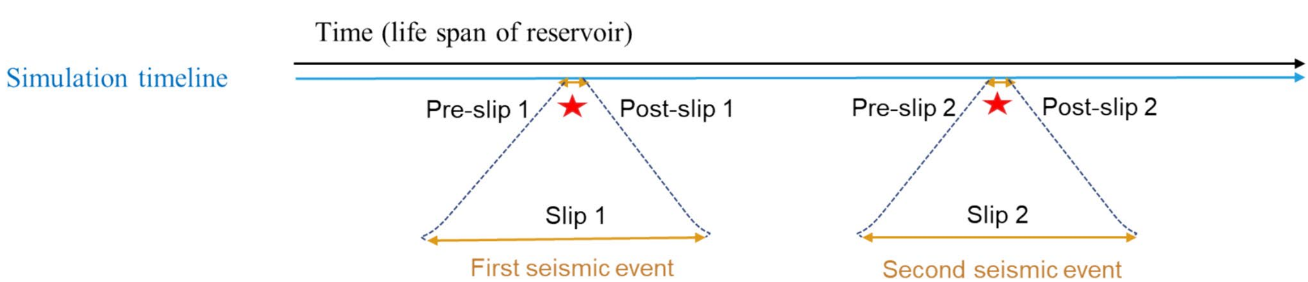

Fig. 3 Timeline of the simulation of the first two seismic events (red stars) induced by the fluid injection into the fault. The different stages of the simulation workflow (numbers) are described in the text with their results: prior to first seismic event (pre-slip 1), during seismic event (reactivation phase) (slip 1), after reactivation and back in the THM simulation (post-slip 1), prior to the second event (slip 2), during second event (slip 2) and, after the earthquake, back in the THM simulation (post-slip 2)

Table 4 Characteristics of the first two induced events

Event No.	Event characteristics			
	Event time (day)	Location (m) (X, Y, Z)	Magnitude (M_w)	Focal mechanism (strike, dip, rake)
E1	1222d	(0, 0, - 1000)	-1	(45°, 90°, 0°)
E2	1222d + 2h	(0.074, 0.074, -999.62)	-0.67	(45°, 90°, 0°)

Fig. 4 Depth profile of temperature (purple dotted), pore pressure (black) and stress components (pink: stress xx, green: stress yy, cyan: stress zz) at the center of the model after the consolidation: **a**: along the whole depth, i.e., [AC] segment or **b**: along the [AB] fault segment

a)

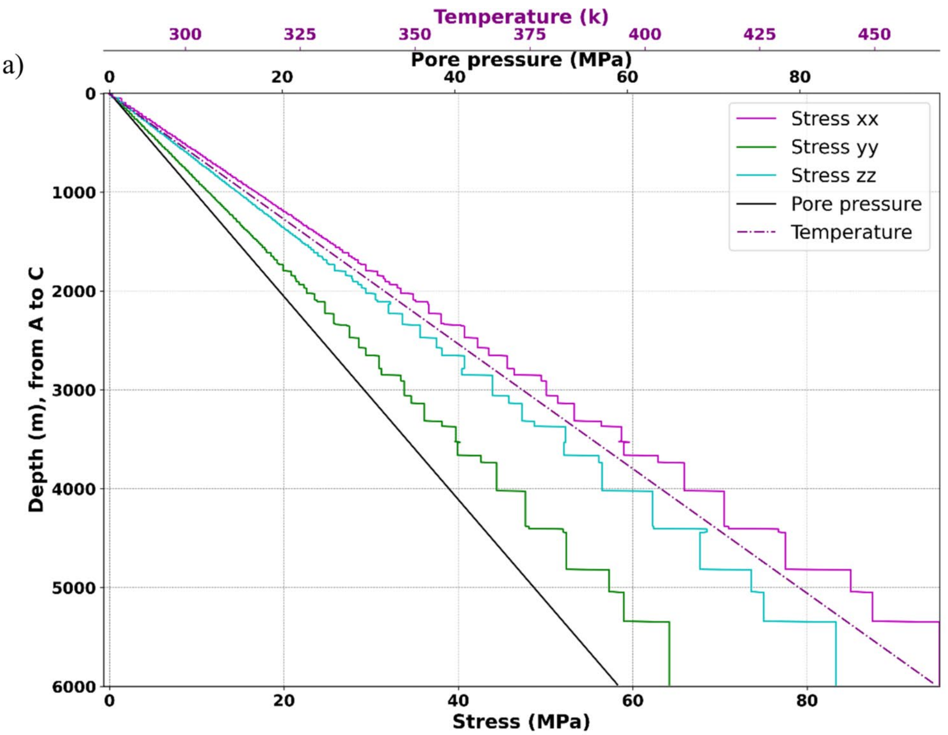

b)

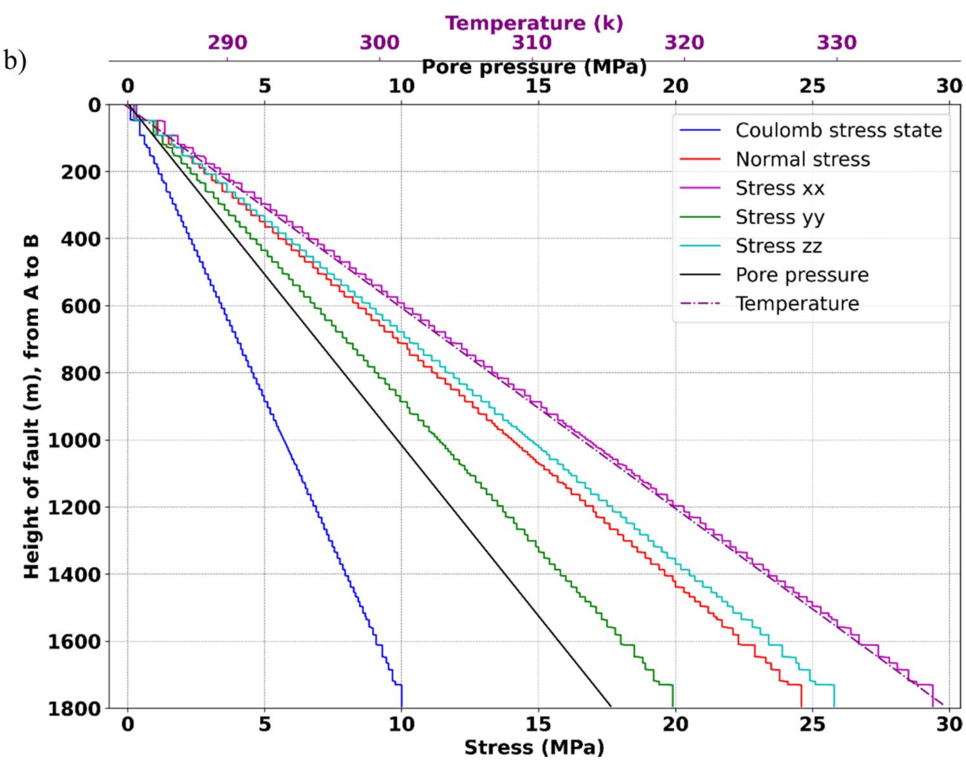

comparing the normal, shear, and Coulomb stresses changes at the reactivation time (last time step in TIGER) and in the first time step of SeisSol. Figure 6a shows the differences of normal, shear and Coulomb stress changes over depth along the [AB] fault segment closed up around the injection point, which confirms that the stress data can be transferred from TIGER to SeisSol with minor errors between stages pre-slip 1 and slip 1. The differences between the stresses before and after projection is smaller than 1 Pa. Moreover, Fig. 6b shows the conversion error in Coulomb stress changes

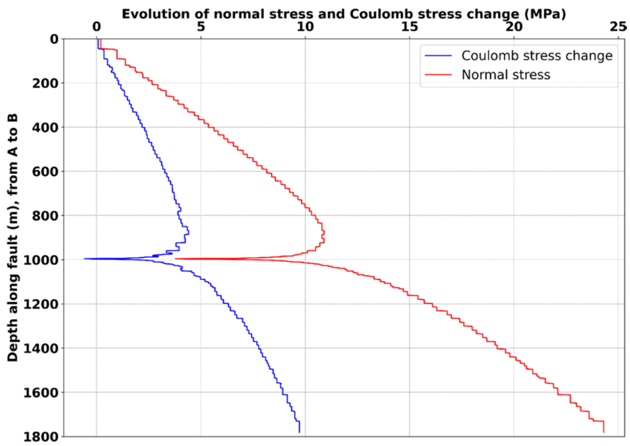

Fig. 5 Normal and Coulomb stresses change over the depth, along the [AB] fault segment, at the reactivation time

resulting from the regridding and interpolation procedure coupling Tiger to SeisSol. The accuracy of the conversion is quantified using the percent error with respect to the target value. The percent error is defined as

$$Error : \left| \frac{u_{target} - u_{converted}}{u_{target}} \right| \times 100,$$

where u_{target} denotes the target stress value and $u_{converted}$ represents the converted stress value. This definition provides a dimensionless measure of the deviation between target and converted values, enabling a consistent comparison across different spatial locations. This comparison is taken before the first event over a 600×600 m^2 fault region centered on the injection point, corresponding to the region of the highest pressure gradient and finest mesh resolution. The absolute error does not exceed 5% even in the regions farthest from the injection point, where element sizes are coarser. This is acceptable, given that the typical stress changes induced by injection are on the order of 2MPa. This confirms that the conversion preserves the stress field accurately for subsequent dynamic rupture simulations.

4.3 Slip 1

The induced seismic event is simulated in SeisSol for 10 s. This duration is long enough to guarantee that the stress changes induced by the dynamic rupture reach a near steady state near the fault and while remaining short enough to minimize computing time. In this synthetic study, we do not focus on the seismic waveforms generated by the rupture. Figure 7 shows the stress changes induced by the seismic event for the three diagonal components at the hypocenter depth (1000 m). The seismic event has a M_W-1 magnitude, and results in stress changes of less than 1 MPa. All stress components show the same polarity pattern, which is representative of the event focal mechanism. As seen from the compression zones (red zones) in the northwest and southeast quartiles around the fault and the extension zones (blue zones) in the northeast and southwest quartiles, a right-lateral strike-slip event is induced.

4.4 Slip 1—Post-Slip 1

The stress changes induced by the seismic event, computed in SeisSol, are added to update the stress field in the TIGER quasi-static simulation. To this end, the SeisSol stress field is first converted from HDF5 to Exodus format, and imported into TIGER using the SolutionUserObject available in MOOSE. The stress change is then added via a MOOSE ParsedFunction to the TIGER stress field from the end of pre-slip 1, i.e., the last stress field prior to reactivation.

TIGER then is run with this updated “initial” stress field, but without resuming injection, until a new equilibrium state is reached. In this phase, the model is allowed to readjust toward equilibrium, which may involve evolution of the displacement field. This step is necessary to balance the stress perturbation induced by the seismic event in the THM model. Figure 8 illustrates the change of the displacement field along and across the fault after the seismic event, i.e., between the reactivation time of pre-slip 1 and post-slip 1. Figure 8a shows a horizontal section of the fault-normal displacement changes resulting from the coseismic motion around the hypocenter (at 1000 m depth) and, similarly, Fig. 8b illustrates the fault-parallel displacement changes. The orientation of the deformation field is consistent with the right-lateral strike-slip event with positive NE-directed displacement along the western side of the fault.

While the stress change is confined to a small rupture zone, displacement appears over a broader area, more than 400 m along the fault. Although this apparent mismatch could partly arise from the visualization scale, it is in fact a consequence of elastodynamic theory and Green’s function solutions for point dislocations in an elastic half-space (Madariaga 1976; Freund 1998; Aki and Richards 2002). Specifically, the far-field displacement field resulting from a localized rupture decays with distance as $\frac{1}{r}$ in 3D-elastic media, whereas the corresponding stress changes decay more rapidly, typically as $\frac{1}{r^2}$ or faster. This difference arises, because stress is related to the spatial derivative of displacement, making its spatial decay inherently steeper.

4.5 Pre-slip 2 and Pre-slip 2—Slip 2

Once the THM model has been re-equilibrated with the updated stress, the injection resumes with the same flow rate (20 L/s) until the next event is triggered. We assume that any mesh a)

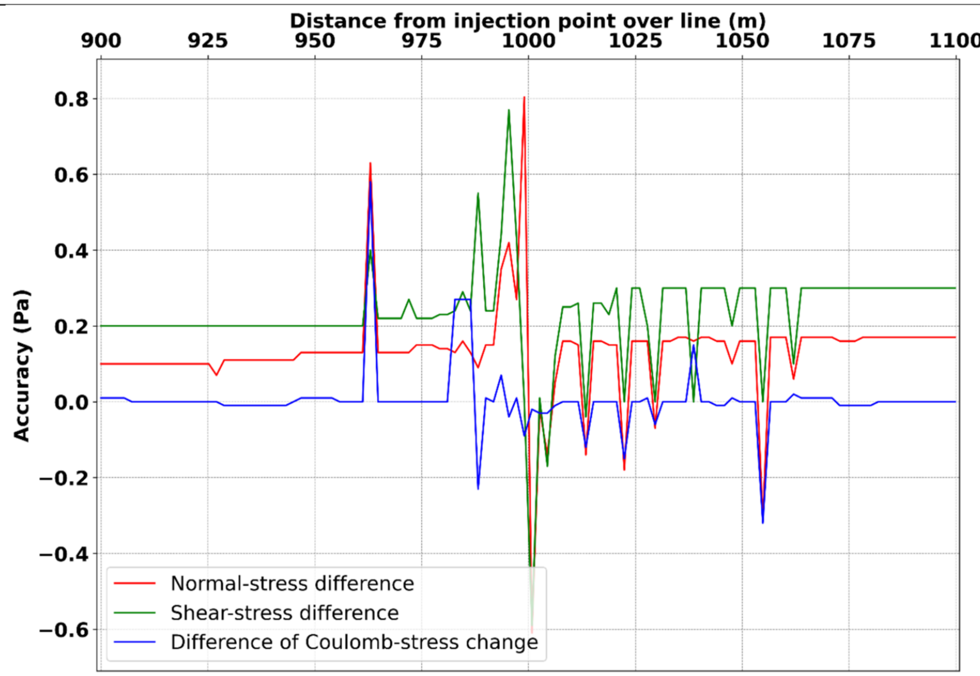

Distance from injection point over line (m)
900
925
950
975
1000
1025
1050
1075
1100
Accuracy (Pa)
0.8
0.6
0.4
0.2
0.0
−0.2
−0.4
−0.6
Normal-stress difference
Shear-stress difference
Difference of Coulomb-stress change

b)

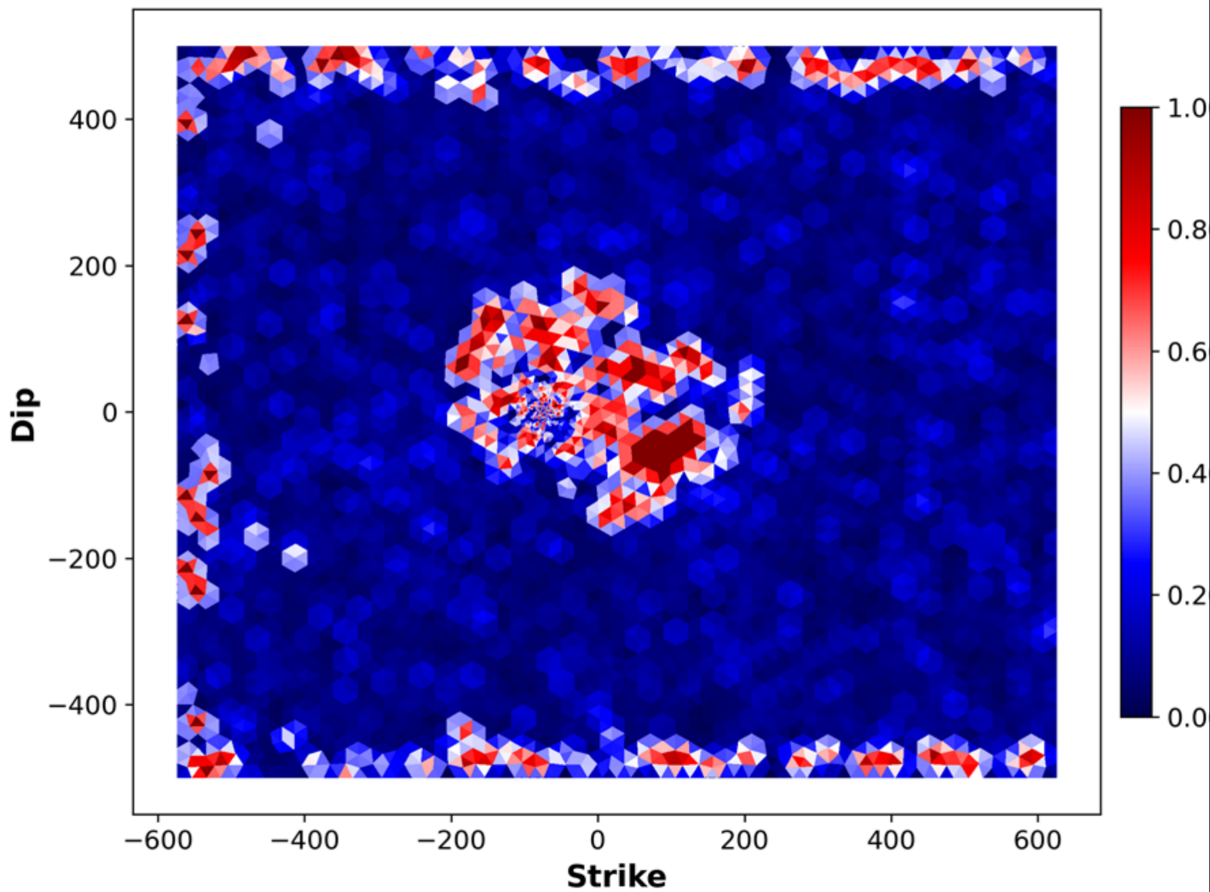

Dip
400
200
0
−200
−400
Strike
−600
−400
−200
0
200
400
600
1.0
0.8
0.6
0.4
0.2
0.0

◀**Fig. 6** **a** Difference of the normal, shear, and Coulomb stress changes between the first time step of SeisSol (slip 1) and the last time step of TIGER (pre-slip 1), along the [AB] fault segment and around the injection point (at 1000 m depth). **b** Spatial distribution of the conversion error between the first time step of SeisSol and the last time step of TIGER over a 600*600 m2 fault patch (centered on the injection point). The error is computed as the absolute relative difference, highlighting deviations across the domain and demonstrating the accuracy of the conversion

element that was fractured in a previous seismic event cannot break again. To implement this numerically, such elements are identified in the mesh, and the Mohr–Coulomb failure criterion is no longer evaluated for them. In this way, the simulation treats these elements as "already broken," ensuring that they do not trigger any subsequent rupture detection.

Following the first event, after nearly 2 h of injection, an element at (0.074, 0.074, –999.62), which had not met the failure criterion in the earlier stages, now becomes critically stressed. This marks the initiation of the second event and the end of pre-slip 2. As at the end of pre-slip 1, TIGER stops and the stress field is transferred to SeisSol. Like Fig. 6, a comparison is performed between the normal, shear, and Coulomb stresses calculated in TIGER at the reactivation moment (last time step) and at initialization (first time step) of SeisSol. These results are not shown here to avoid redundancy.

4.6 Slip 2

The simulation workflow in slip 2 is similar to that in slip 1. SeisSol runs for 10 s to simulate the dynamic rupture of the second seismic event. The second event, with a M_W -0.67 magnitude, is slightly larger than the first one. As shown in Fig. 9, the stress change components have a similar pattern to the first event. Hence, the movement of the fault is comparable, still a right-lateral strike-slip. However, the magnitudes and extent are larger. We intentionally used the same viewing perspective and color scale for Figs. 9 and 7 to emphasize the differences.

4.7 Slip 2—Post-slip 2 and Post-slip 2

Following the second event, the stress field in TIGER is updated using the stress changes output by SeisSol and the displacements associated with the dynamic rupture calculated before resuming the geothermal fluid injection. Figure 10a, b shows the coseismic displacements across and along the fault, respectively, on a horizontal section crossing the hypocenter (-999.62 m depth). This highlights the right-lateral strike-slip nature of the second event.

5 Discussion

In the following, we discuss constraints associated with the numerical implementation of the coupling as well as physical assumptions that may affect the interpretation and limit the modeling approach. We also highlight potential extensions of the framework and opportunities for further developments, aimed at improving model realism and enhancing its application to forecasting and risk assessment.

5.1 Numerical Implementation of the Workflow

In the MOOSE framework, a variable can be defined either as an elemental or a nodal variable. The theoretical difference between them is that a nodal variable has its values stored at the node of an element (in FE techniques) and is interpolated across elements using the nodal finite-element shape functions, while an elemental variable has its values stored at one or several quadrature points within the element, depending of the polynomial degree of the basis function. In our TIGER models, as in MOOSE per default, the stress tensor variables are defined as elemental material properties of polynomial degree 0. This allows efficient computation with other elemental material properties (e.g., elasticity tensor, thermal expansion, etc.) and avoids applying a projection method to transfer a value from the node to the element or vice versa in the THM model, which can may introduce interpolation artifacts and degrade numerical accuracy.

Using an element constant stress variable comes with the limitation that the magnitude of the stress value at a given point strongly depends on the local mesh size and resolution. When the mesh is coarse or the stress varies spatially significantly around a given point, large difference can appear between the stress values of nearby elements. This explains the step-wise stress profiles (numerical artifact) in Fig. 7a. The mesh size around the fault is reduced to avoid this stepping. We note that the potential presence of such artifacts is much more critical around the fault than at the bottom of the model, where pronounced step-wise stress profile can be safely ignored. Overall, given the fine mesh resolution, and our choice of degree-0 basis functions in TIGER does impact significantly numerical and code coupling accuracy, given the fine mesh resolution.

We note that SeisSol implements a quadrature free approach in which element mass and stiffness matrix are computed analytically. Therefore, the solved quantities can be evaluated with similar accuracy anywhere in the element. On the other hand, fault friction (and the fault tractions it depends on) is evaluated at quadrature points on the fault, which are typically much denser

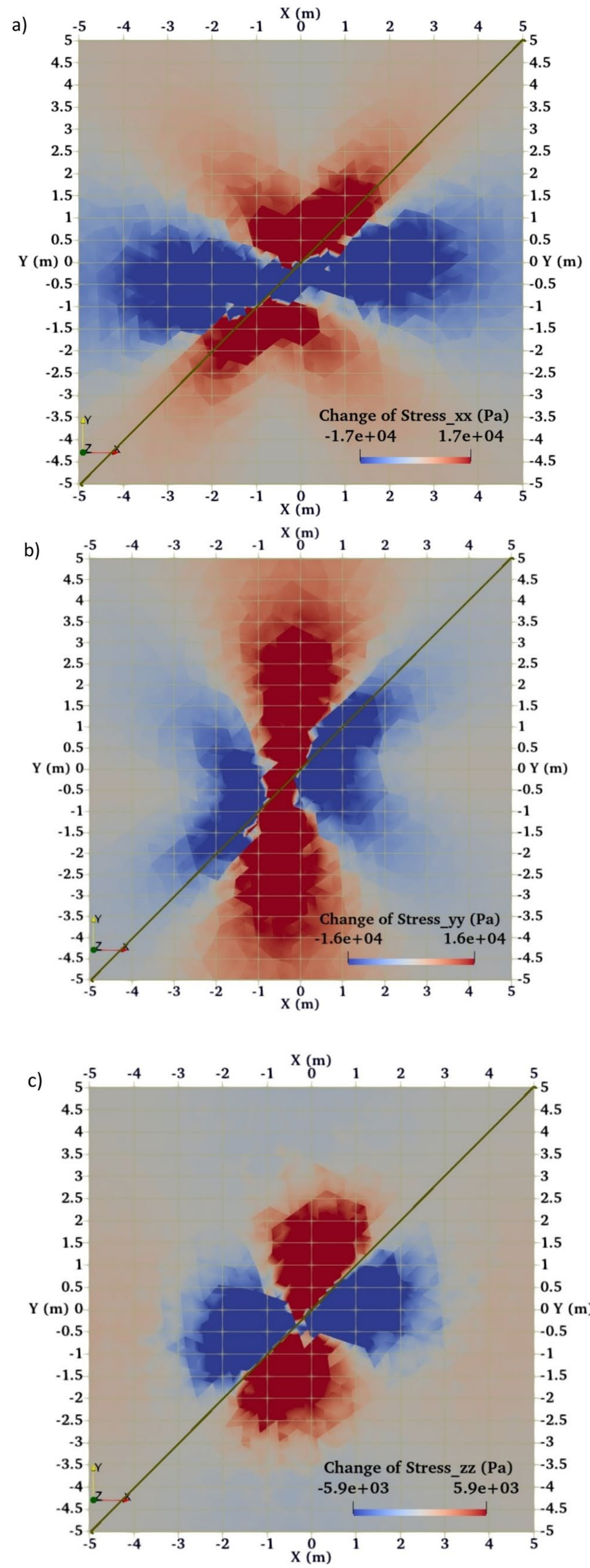

Fig. 7 Magnitude of stress changes induced by the first seismic event as calculated in SeisSol: **a** stress-xx, **b** stress-yy, and **c** stress-zz

than the quadrature points in TIGER, due to the high polynomial degree basis function used in SeisSol.

It is worth mentioning that TIGER solves the THM problem using continuous Galerkin finite elements, while SeisSol features discontinuous Galerkin finite elements. Such a discrepancy is challenging for the developed approach. In fact, SeisSol calculates stress change in 3D elements while the fault is a 2D interface across which stress drop (discontinuity) occurs during rupture. On the other hand, stress must be continuous across the fault in TIGER. Hence, to transfer the stress changes from SeisSol to TIGER, the stress changes of SeisSol are used to initialize the stress changes in the 3D elements of TIGER and subsequently mapped into a continuous field on the 2D elements of the fault. Such a coupling introduces a kinematic incompatibility: SeisSol permits displacement jumps across the fault during dynamic rupture, while TIGER enforces displacement continuity. After transferring the post-slip stress field from SeisSol back to TIGER, a quasi-static re-equilibration step is performed to project the stress state onto TIGER's continuous displacement space. This re-equilibration solves the static equilibrium equation with the transferred stress as initial condition, allowing the system to relax to a compatible state before the next quasi-static loading increment. Mathematically, this is equivalent to treating the dynamic slip as a strain localized on the fault interface, which is then homogenized into the continuum framework. While this introduces a numerical artifact, we minimize its impact through fine fault-zone meshing (element size ~10 cm) and coupling time steps small enough to limit slip increments per event. Figure 13 shows that the stress transfer after the event between both sides of the fault is reasonably reliable. A more rigorous approach would involve implementing displacement discontinuity directly within TIGER.

TIGER combines elements of different dimensions (3D tetrahedra, 2D fault triangles and 0D injection points). Nodal variables that are explicitly shared between domains (e.g., pressure) transfer directly through the shared nodes. However, volumetric variables that are evaluated over the element (e.g., stress) are typically represented by projection onto element quadrature points. In our workflow, the 3D stress field is computed in the volume and then projected onto the 2D fault surface. Because 3D tetrahedra and 2D triangles generally use different quadrature rules and different numbers/locations of integration points, straightforward sampling can produce apparent step-wise transitions when the 2D fault triangle is attached to a 3D tetrahedron with more quadrature points. Theoretically, to avoid this issue, the governing equations containing elemental variables should be adapted to the dimension of the element considered and discretized on the involved domain (Keilegavlen et al. 2019; Koch 2020). In our approach, along the fault, 2D triangle

Fig. 8 Horizontal section at the injection point (1000 m depth) of the coseismic displacement field induced by the first seismic event: **a** across the fault and **b** along the fault

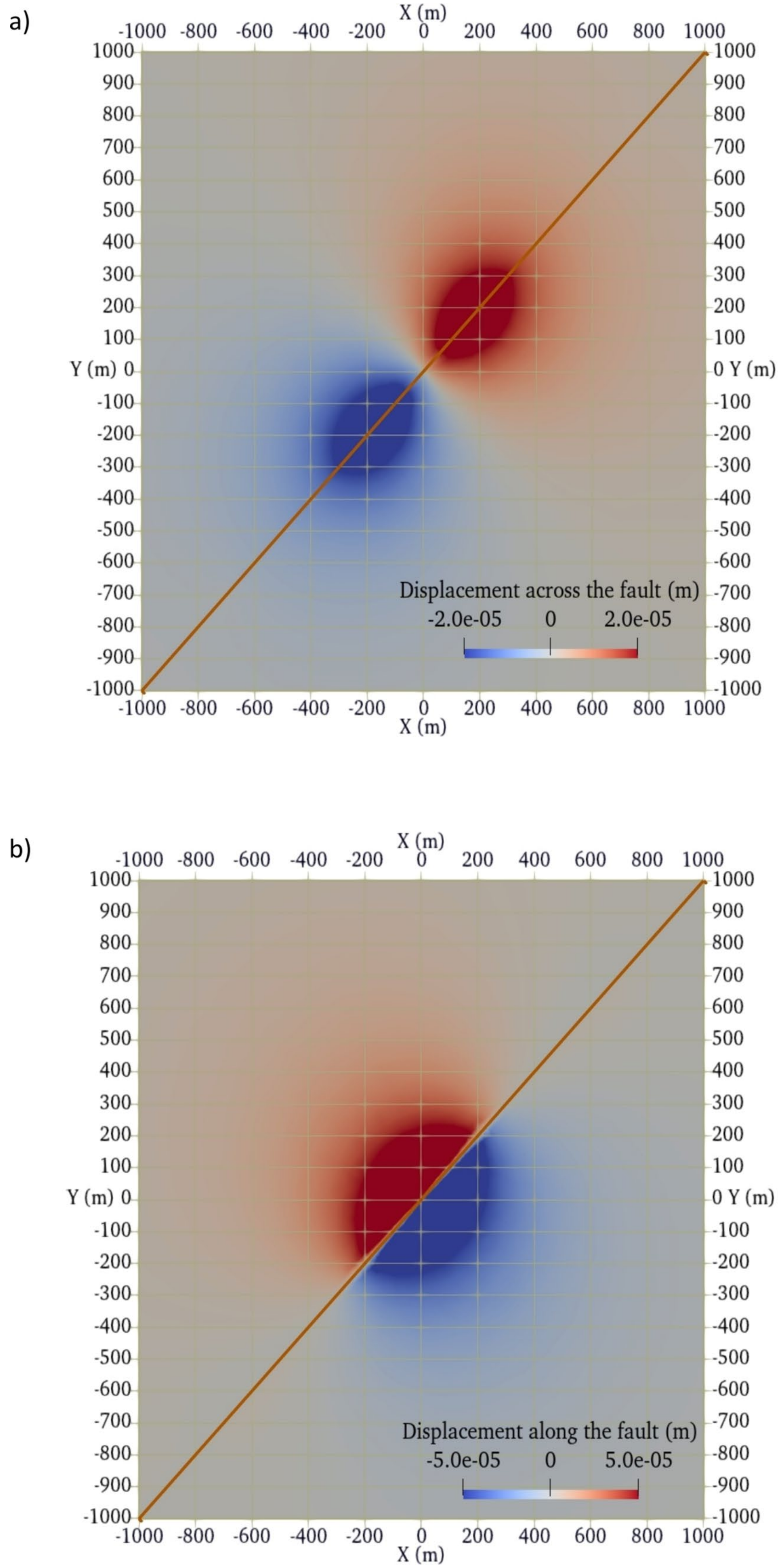

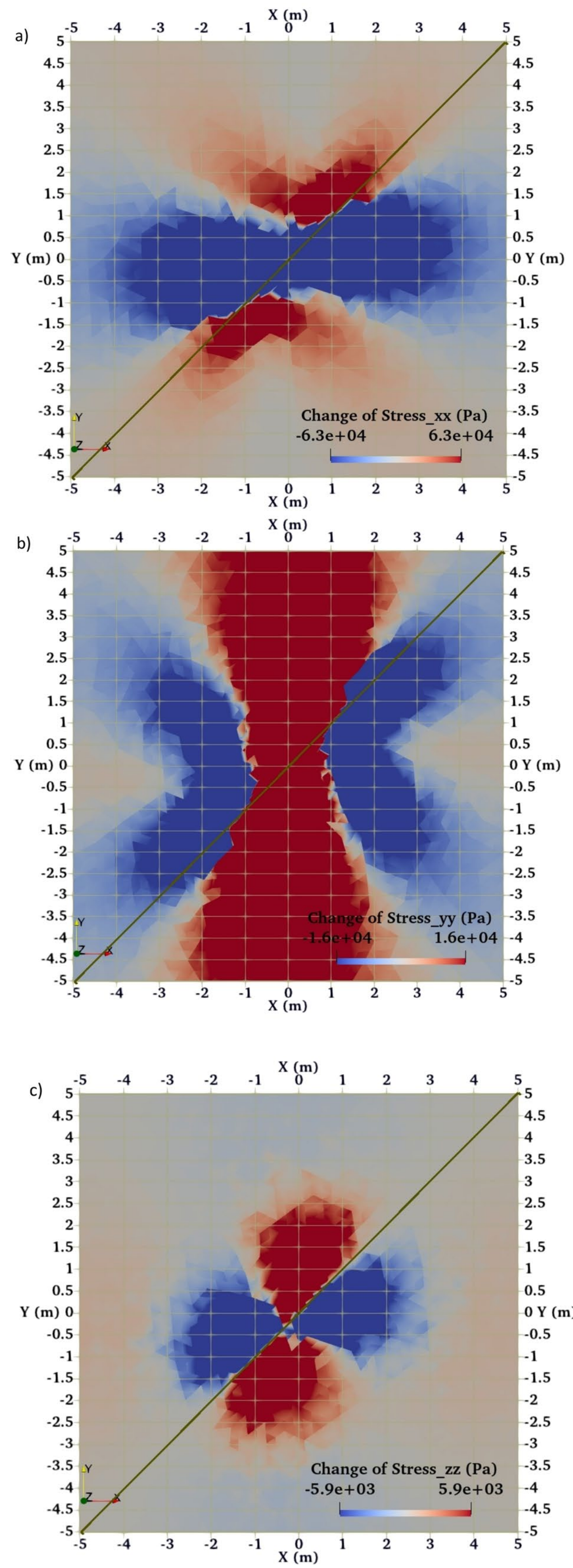

Fig. 9 Magnitudes of stress changes induced by the second seismic ▶ event as calculated in SeisSol: **a** stress-xx, **b** stress-yy, and **c** stress-zz

elements (with one quadrature point) are interfaced with their surrounding 3D tetrahedra (each using several quadrature points). The difference in integration schemes between the two element types leads to slightly inconsistent values of elemental variables across the interface. Increasing the mesh resolution around the fault interface mitigated this artifact by smoothing the transition of these quantities between elements of different dimensions.

Stress changes due to the induced seismicity could be relatively large and lead to significant differences between the stress field at the last time step of TIGER and the updated stress field. Such abrupt changes could cause numerical difficulties in the quasi-static model, potentially preventing convergence to a steady state when the new stress state is applied in TIGER (slip 1—post-slip 1). In our approach, the user can take control of each processing stage before starting it, if necessary. In this particular situation, the duration of the initial time step could be decreased to manage convergence in TIGER. However, this manual tuning is not realistic for simulations involving thousands of events over long stimulation periods (e.g., a 1-day EGS operation). To deal with it, for example, an adaptive control mechanism could be added, able to monitor residuals or stress increments and dynamically modify simulation parameters, such as time step size or solver tolerances, without user intervention. This would significantly enhance the robustness and scalability of the coupled workflow for realistic field-scale applications.

Although the case study we showcase are characterized by limited complexity in terms of the number of faults and their geometries, and assume a near-critically stressed initial state allowing a short time to fault reactivation, the framework we developed is explicitly designed for field-scale, decadal simulations. In fact, parallel scalability enabled in Tiger through MOOSE's PETSc-backed domain decomposition and implicit Newton–Krylov solvers, which scale efficiently to thousands of cores, as well as in SeisSol by end-to-end optimization targeting recent HPC systems (Heinecke et al. 2014; Uphoff et al. 2017; Krenz et al. 2021a, b; Dorozhinskii 2024), enables modeling larger real-case studies over longer time frames. In addition, static mesh adaptivity and the dimension reduction approach implemented in Tiger allow the use of a high-quality mesh with a constrained number of elements, reducing the time to solution. Adaptive time-stepping combined with the implicit time integration implemented in Tiger and checkpointing capabilities ensures the long-term stability of the simulation and further constrains the time to solution.

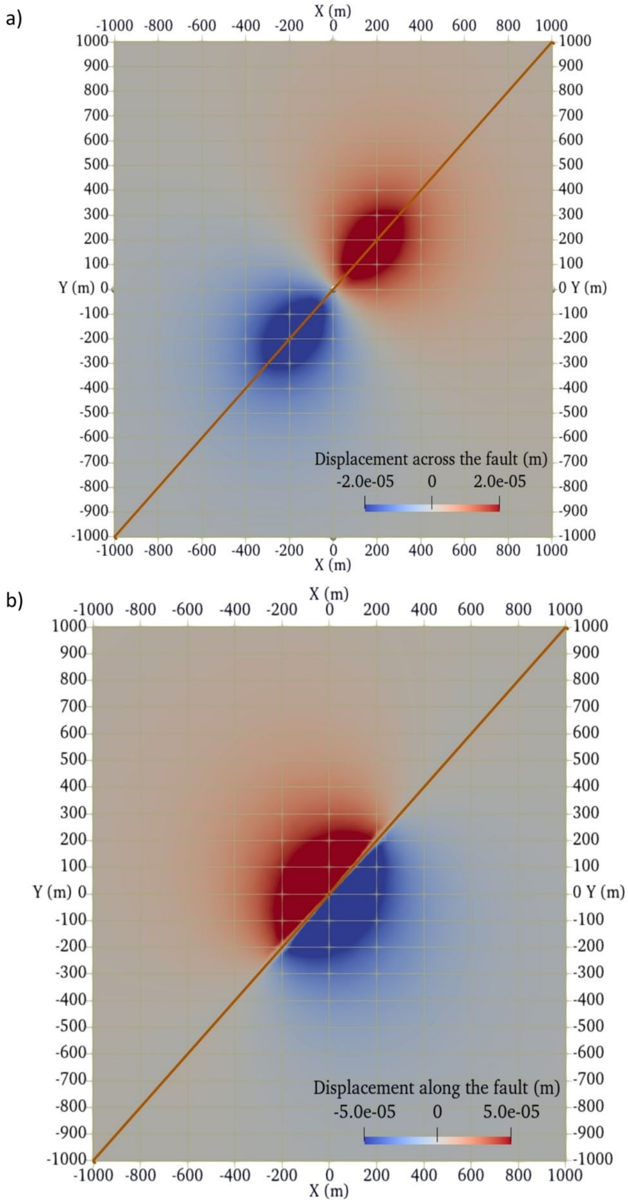

Fig. 10 Horizontal section at the injection point (1000 m depth) of the coseismic displacement field induced by the second seismic event: **a** across the fault and **b** along the fault

5.2 Friction Heterogeneity

In this work, we did not apply a heterogeneous friction coefficient, although both TIGER and SeisSol already support this capability. This variability could be assigned stochastically to represent aspects of fault complexity, improving the physical realism of the reactivation process, as natural faults are rarely uniform. It would also enable the study of rupture nucleation at weak patches and more complex seismic sequences such as foreshock–mainshock patterns, contributing to a deeper understanding of fault behavior in geothermal systems.

5.3 Thermal and Hydraulic Feedback

Currently, our coupled modeling framework only transfers stress changes from SeisSol to TIGER, while other dynamically evolving properties, such as permeability and friction coefficients, remain unchanged between events. This is a simplification, since properties like permeability, friction, and even temperature can evolve rapidly during fault slip (Liu and Manga 2009; Manga et al. 2012). In particular, shearing may release heat, potentially leading to localized temperature increases that could affect hydro-mechanical behavior. These coseismic thermal effects are not currently transferred back into the quasi-static model (TIGER). In other words, in the current version of the framework, the quasi-static thermal effects are included in the quasi-static simulator through cold water injection; however, the dynamic thermal effects due to shearing, for example, are not considered. Despite this limitation, the sequential nature of the coupling, where SeisSol and TIGER run in series, offers a flexible foundation to incorporate additional state variables (e.g., permeability or temperature) in future implementations. Updating these properties after each event, based on physically motivated rules or empirical relations, would enhance realism without requiring simultaneous time integration.

However, fully capturing these transient processes would require a much stronger coupling between the simulators, solving the governing equations of dynamic rupture and hydro-mechanics in parallel. While strong coupling is theoretically appealing, it remains methodologically and computationally complex.

5.4 Seismic hazard modeling

We demonstrated that the proposed coupled approach (using TIGER for quasi-static THM processes and SeisSol for dynamic rupture) can generate a seismicity catalog by simulating multiple fault reactivation events under realistic reservoir conditions. A full quantitative validation of the coupled THM–dynamic rupture framework is not feasible at present, as no benchmark solutions exist for this level of multiphysics coupling. Instead, the current study focuses on verifying the physical consistency of the approach. Several checks support the robustness of the implementation: (i) stress transfer between the quasi-static and dynamic solvers introduces negligible errors, (ii) the resulting displacement field is consistent with expected mechanical behavior, and (iii) the simulated focal mechanisms align with stress conditions and patterns reported in the literature. These results indicate that, while quantitative validation remains an open challenge, the coupled framework reproduces physically meaningful behavior and provides a reliable tool for exploring induced seismicity in complex systems. For example, despite the presented model used a simplified geometry with a planar fault and uniform injection, the methodology is applicable to more complex scenarios, including non-planar fault surfaces and heterogeneous injection schemes. These enhancements would produce a more representative synthetic seismicity catalog, potentially matching field observations. The framework's field-scale capabilities could be validated through application to a real geothermal site, such as the Soultz-sous-Forêts or Basel projects. Although our study did not leverage the full capabilities of SeisSol, such as surface displacement modeling or high-resolution ground motion simulations (e.g., (Taufiqurrahman et al. 2022)), this remains an important opportunity. Leveraging this in our coupling scheme would allow direct modeling of ground motion and seismic intensity at the surface for selected seismic event, a critical factor for induced seismicity risk assessment and communication with stakeholders. Our serial coupling setup provides flexibility, allowing the user to monitor and manage each step, for example, adjusting time step sizes in TIGER following large stress changes from dynamic rupture.

Overall, this approach lays the foundation for a predictive, physics-based simulation pipeline for induced seismicity in geothermal systems. Future developments should include updating material properties (e.g., permeability, friction) based on fault slip and stress history, and incorporating thermally driven processes such as thermal pressurization. Besides, having considered the development of alternative approaches, such as Phase-Field Modeling (PFM) (Xu et al. 2024b, a; Xu et al. 2026), which has recently proven suitable for simulating fracture propagation in reservoir geomechanics, enables modeling of complex crack initiation, branching, and coalescence without explicit re-meshing or surface tracking.), This approach could be integrated into a coupled THM–seismicity framework similar to the one presented here, allowing for studies that simulate evolving fracture networks and more complex fracturing scenarios, beyond pre-existing faults. While a fully coupled THM–dynamic rupture solver remains a long-term goal, the current framework can be expanded incrementally to improve realism and operational value.

6 Conclusion

In this study, we propose a new approach to model the coupled quasi-static THM processes and dynamic rupture response of a faulted geothermal reservoir under operational conditions. The methodology involves coupling two state-of-the-art open-source software packages: TIGER (based on MOOSE) for simulating the 3D THM response of the reservoir and SeisSol for simulating the 3D dynamic rupture process on the fault and the associated stress field in the surrounding medium.

Code-coupling is implemented in a serial manner: the simulation begins with TIGER under predefined initial and boundary conditions. Once the reactivation condition is met, the critical stress state is transferred to SeisSol, which simulates the dynamic rupture of the seismic event. The resulting stress changes are then transferred back to TIGER, updating the stress field for continued fluid circulation modeling. This stage updates the stress field in the fluid circulation model based on the stress change of the dynamic model which completes one loop of the coupled workflow. To automate data exchange, manage simulations, and archive outputs, a workflow automation script was developed. To validate our method's capability, a simple synthetic model with a faulted reservoir is created in which we model reservoir and injection operations and dynamic rupture. Two seismic events are simulated using two loops of our coupling approach. Each event's results are analyzed across three stages: before the seismic event, during dynamic rupture, and after the event. The results show that the method successfully captures the interaction between geothermal operations and fault rupture dynamics, including stress redistribution due to induced seismicity.

This approach is suitable for application to field-scale cases, offering a way to verify and deepen understanding of coupled fluid-induced seismic processes in geothermal systems. The modular, automatable design of the framework allows for future integration with high-performance computing workflows and ensemble modeling strategies. Future improvements could incorporate dynamic permeability changes, rate-and-state friction, or thermal pressurization to more accurately capture fault response under varying operational scenarios.

Appendix: Review of Existing Numerical Code for Simulating Induced Seismicity

Over the past decade, several studies have reviewed and classified numerical tools for modeling subsurface energy systems and induced seismicity, highlighting their applicability, underlying physics, and capabilities. In 2011, Rutqvist (2011) explained and listed numerical tools for modeling subsurface energy systems (e.g., oil and gas industry, geothermal, CO2 sequestration, etc.) based on their applicability, physics, and equations involved. More recently, Song et al. (2023) listed numerical tools specifically used for modeling induced seismicity in CO2 storage. In Table 5, we present an updated list of physics-based numerical tools applied to simulate induced seismicity in geothermal systems, including several that were discussed in the previous paragraphs. The table shows the strengths and limitations of each code for geothermal system modeling and indicates whether they can simulate injection operations to fault failure (FF), dynamic rupture propagation (RP), or feedback effects (FB) enabling models of multiple-event sequences.

Table 5 List of proprietary (PROP) or free and open-source software (FOSS) or numerical frameworks available for modeling induced seismicity in geothermal fields. The main features are provided as well as the extent to which induced seismicity is modeled: FF for modeling injection operations to fault failure, RP for dynamic rupture propagation, and FB for feedback effects enabling modeling of multiple-event sequences. Examples of application are also listed

Software/ framework	Main features		Seismicity modeling			Example	License
			FF	RP	FB		
TOUGH-FLAC	Multiphase fluid and heat flow simulation Geochemical interactions Natural fracture in porous media modeling. Supports heterogeneous porosity and permeability conditions Poroelasticity Injection/production modeling		Yes	–	–	Rutqvist and Oldenburg (2007) introduced the software and applied it to Geyser Geothermal Field to determine the critical reactivation state due to operation.	PROP
COMSOL Multiphysics	Coupled physics including modules for geomechanics and subsurface flow. Predefined multiphysics interfaces that simplify the setup of coupled problems Comprehensive material library and feasibility to define custom material properties Injection/production modeling Wave propagation modeling		Yes	–	–	Chang and Yoon (2022) applied COMSOL to model the triggering potential along faults due to operation.	PROP
ABAQUS	Robust simulation capabilities for geomechanical modeling and fluid-structure interaction. Feasibility to couple multiphysics e.g., heat transfer, fluid flow Transient and steady-state simulation		Yes	–	–	He et al. (2022) analyzed hydromechanically the injection-induced fault activation using ABAQUS.	PROP
GEM-COM-SOL	Probabilistic seismic hazard analysis and risk assessments. Supports heterogeneous porosity and permeability conditions Injection/production modeling Multiphysics including fluid flow, heat transfer, and geomechanics		Yes	–	–	Khan et al. (2020) determined fault reactivation in the Biyadh sandstone reservoir (CO2 storage) in Saudi Arabia.	PROP
PFC3D	Multi-scale modeling of thermo-hydro-mechanical behavior of fracture/fault. Contact mechanics with complicated friction law Customizable material models		Yes	–	–	Park and Song (2009) studied shearing behavior and failure process of rock joints through direct shear tests and investigated affecting parameters such as friction coefficient.	PROP
FracMan	Creating and analyzing discrete fracture networks. Stochastic and deterministic approaches for fracture modeling Interaction thermo-hydro-mechanical impact of fracture networks Integrating discrete fracture networks with continuum-based reservoir models		Yes	–	–	Shan et al. (2023) applied FracMan to study the magnitude and distribution range of the microseisms induced by hydraulic fracturing as a function of the existence of faults, in-situ stress state, fracture occurrence, and fracture distribution near faults.	PROP
MOOSE framework	Coupled multiphysics simulations, simultaneous modeling of thermal, hydraulic, mechanical, and chemical processes Predefined modules and material properties for common physics specifically for geothermal applications Multi-scale modeling of thermo-hydro-mechanical behavior of fracture/fault. Simulation of fracture initiation, propagation, and interaction Multiphase and multi-component flow simulations	FALCON	Yes	–	–	Podgorney et al. (2021) applied FALCON (a MOOSE-based App) to simulate the THM response of the Utah FORGE Enhanced Geothermal Site.	FOSS
		GOLEM	Yes	–	–	Cacace et al. (2021) Applied Golem for induced seismicity forecasting by linking frictional Coulomb stress changes to seismic hazard, capturing the effects of fluid pressure and temperature.	
		TIGER	Yes	–	–	See Section 2 for more details.	
Itasca's 3DEC	Discrete element framework, allowing calculating interactions between blocks, including contact forces and displacements Multi-scale modeling of thermo-hydro-mechanical behavior of fracture/fault. Customizable Material Models		Yes	–	–	Yin et al. (2020) studied fault reactivation and induced seismicity during fracturing and backflow in hydraulic fracturing.	PROP
PyLith	Simulation coupled physics including thermal, mechanical, and fluid flow processes Supports predefined and custom physics modules and material properties Simulating the initiation and propagation of faults and fractures		Yes	–	Yes	Walker et al. (2023) introduced the latest version including poroelasticity, and possibility of combining with quasi-static and dynamic modeling of faulting. No thermal modeling.	FOSS

Table 5 (continued)

Software/framework	Main features	Seismicity modeling			Example	License
		FF	RP	FB		
TOUGH-PyLith	Adds support for modeling multiphase fluid, heat transport, and geochemical interactions to PyLith's capabilities	Yes	–	–	Blanco-Martín et al. (2022) evaluated the potential risk of fault reactivation in NER300 ULCOS CO2 storage project.	PROP
GEOS	Coupled simulations of thermal, hydrological, mechanical, and chemical processes Customizable and extendable modular design Time-evolving porosity and permeability during the simulation Modeling chemical reactions and transport processes as well as the effects of mineral dissolution and precipitation on reservoir properties	Yes	–	–	Fei et al. (2023) utilized GEOS to model fracture nucleation and propagation process of hydraulic fractures around boreholes.	FOSS
Eclipse-VISAGE	Modeling the impact of fluid extraction and injection on reservoir stability and seismicity Phase behavior phenomena such as phase transitions (e.g., vapor-liquid equilibrium) and phase changes (e.g., boiling and condensation) Supports dual-porosity and dual-permeability modeling approaches Supports failure criteria for transition between elastic and plastic behavior	Yes	–	–	Savvatis et al. (2019) performed THM simulation on a geothermal reservoir in the Molasse basin (Germany) to investigate the potential of seismic events due to operation.	PROP
SeisSol	Simulating viscoelastic and poroelastic seismic wave propagation in complex geological structures, coupled with earthquake rupture on arbitrary complex fault structures. Supports tetrahedral meshes Supports heterogeneous media Supports complex friction law, e.g., rate-and-state friction laws	–	Yes	–	Palgunadi et al. (2020) applied SeisSol to constrain the conditions that lead to the Pohang earthquake, South Korea, in the geothermal site due to high rate injection.	FOSS
GeoSys/Rockflow	Simulating the coupled interactions between thermal, hydraulic, mechanical, and chemical processes Simulation of multiphase multi-component flow Dual-porosity and dual-permeability models Modeling complex fracture networks and their thermo-hydro-mechanical impact	Yes	–	–	Kolditz et al. (2012) illustrated the capability to model the seismicity potential through failure criteria.	FOSS/PROP
CODE-BRIGHT	Simulating the coupled behavior of fluid flow, heat transfer, and rock mechanics Modeling complex fracture networks and their thermo-hydro-mechanical impact	Yes	–	–	Kivi et al. (2022) performed THM simulation in a hot sedimentary aquifer to investigate the induced seismicity potential.	FOSS

Acknowledgements Rahim Habibi's work was conducted in the frame of the INSIDE project, which was supported by the German Federal Ministry for Economic Affairs and Energy (BMWE) and the Project Management Jülich (PtJ) under grant agreement number 03EE4008C. Rahim Habibi's work is also part of the subtopic "Geoenergy" in the program "MTET–Materials and Technologies for the Energy Transition" of the Helmholtz Association. Thomas Ulrich acknowledges support by the Geothermal-Alliance Bavaria (GAB) project founded by the Bavarian State Ministry for Science and Art. Thomas Ulrich and Alice-Agnes Gabriel acknowledge support from the German Ministry of Research and Education and Horizon Europe (ChEESE-2P, Grant No. 1010930, DT-GEO, Grant No. 101058129 and Geo-INQUIRE, Grant No. 101058518). Alice-Agnes Gabriel acknowledges additional support from the National Science Foundation (NSF Grant Nos. CRESCENT EAR-2225286, MTMOD EAR-2121568, LCCF-CSA OAC-2323116, QUAKEWORX OAC-2311208), the National Aeronautics and Space Administration (NASA 80NSSC20K0495), and the Statewide California Earthquake Center (SCEC Project Nos. 25259, 25313, 25341).

Author Contributions Rahim Habibi: writing—original draft, editing, methodology, conceptualization, visualization, coding, and simulation. Thomas Ulrich: writing—editing, coding and software, methodology, conceptualization, investigation, and data curation. Alice-Agnes Gabriel: review and editing, methodology, and conceptualization. Thomas Kohl: review and editing, methodology, and conceptualization. Emmanuel Gaucher: review and editing, supervision, methodology, conceptualization, investigation, data curation, and project administration.

Funding Open Access funding enabled and organized by Projekt DEAL. This work was funded by German Federal Ministry for Economic Affairs and Energy (BMWE) and the Project Management Jülich (PtJ) under Grant Agreement No. 03EE4008C. Also part of the subtopic "Geoenergy" in the program "MTET—Materials and Technologies for the Energy Transition, Bavarian State Ministry for Science and Art, as well as support from the German Ministry of Research and Education and Horizon Europe (ChEESE-2P, Grant No. 1010930, DT-GEO, Grant No. 101058129, and Geo-INQUIRE, Grant No. 101058518), German Ministry of Research and Education and Horizon Europe (ChEESE-2P, Grant No. 1010930, DT-GEO, Grant No. 101058129, and Geo-INQUIRE, Grant No. 101058518). Also, there is an additional support from the National Science Foundation (NSF grant numbers CRESCENT).

Data Availability The open-source codes used for this study are openly available in [SeisSol] at [https://github.com/SeisSol/SeisSol] and [TIGER] at [https://zenodo.org/records/15879856] accordingly. The data that support the findings of this study are available in a public repository [Rahim-Habibi/Tiger-SeisSol-public].

Declarations

Conflict of interest The authors declare that they have no known competing financial interests or personal relationships that could have appeared to influence the work reported in this paper.

References

Aagaard BT, Knepley MG, Williams CA (2013) A domain decomposition approach to implementing fault slip in finite-element models of quasi-static and dynamic crustal deformation. J Geophys Res Solid Earth 118:3059–3079. https://doi.org/10.1002/jgrb.50217

Aki K, Richards PG (2002) Quantitative seismology. University Science Books

Altmann JB, Müller TM, Müller BIR et al (2010) Poroelastic contribution to the reservoir stress path. Int J Rock Mech Min Sci 47:1104–1113. https://doi.org/10.1016/j.ijrmms.2010.08.001

Andrews DJ (1976) Rupture propagation with finite stress in antiplane strain. J Geophys Res 1896–1977(81):3575–3582. https://doi.org/10.1029/JB081i020p03575

Atkinson GM, Eaton DW, Igonin N (2020) Developments in understanding seismicity triggered by hydraulic fracturing. Nat Rev Earth Environ 1:264–277. https://doi.org/10.1038/s43017-020-0049-7

Auradou H, Drazer G, Hulin JP, Koplik J (2005) Permeability anisotropy induced by the shear displacement of rough fracture walls. Water Resour Res 41:W09423. https://doi.org/10.1029/2005wr003938

Baisch S, Vörös R (2010) Reservoir induced seismicity: Where, when, why and how strong?

Beeler HS (2004) Stress-induced, time-dependent fracture closure at hydrothermal conditions. J Geophys Res. https://doi.org/10.1029/2002JB001782

Blanco-Martín L, Jahangir E, Rinaldi AP, Rutqvist J (2022) Evaluation of possible reactivation of undetected faults during CO2 injection. Int J Greenhouse Gas Control 121:103794. https://doi.org/10.1016/j.ijggc.2022.103794

Breuer A, Heinecke A, Bader M (2016) Petascale Local Time Stepping for the ADER-DG Finite Element Method. In: 2016 IEEE International Parallel and Distributed Processing Symposium (IPDPS). pp 854–863

Cacace M, Jacquey AB (2017) Flexible parallel implicit modelling of coupled thermal–hydraulic–mechanical processes in fractured rocks. Solid Earth 8:921–941. https://doi.org/10.5194/se-8-921-2017

Cacace M, Hofmann H, Shapiro SA (2021) Projecting seismicity induced by complex alterations of underground stresses with applications to geothermal systems. Sci Rep 11:23560. https://doi.org/10.1038/s41598-021-02857-0

Chang KW, Yoon H (2022) Permeability-controlled migration of induced seismicity to deeper depths near Venus in North Texas. Sci Rep 12:1382. https://doi.org/10.1038/s41598-022-05242-7

Coussy O (2004) Poromechanics|Wiley. Wiley.com

de Jesus AC (2016) 17 - Environmental benefits and challenges associated with geothermal power generation. In: DiPippo R (ed) Geothermal power generation. Woodhead Publishing, pp 477–498

Dorozhinskii R (2024) Adapting and Optimizing High Order Seismic Simulations for GPU-based Supercomputers. Technische Universität München

Dumbser M, Käser M (2006) An arbitrary high-order discontinuous Galerkin method for elastic waves on unstructured meshes — II. The three-dimensional isotropic case. Geophys J Int 167:319–336. https://doi.org/10.1111/j.1365-246X.2006.03120.x

Eberhardt E (2012) The Hoek-Brown failure criterion. Rock Mech Rock Eng 45:981–988. https://doi.org/10.1007/s00603-012-0276-4

Egert R, Nitschke F, Gholami Korzani M, Kohl T (2021) Stochastic 3D Navier-Stokes flow in self-affine fracture geometries controlled by anisotropy and channeling. Geophys Res Lett 48:e2020GL092138. https://doi.org/10.1029/2020GL092138

Egert R (2022) Vergleich von Moose/TIGER und Comsol Multiphysics anhand eines THM Modells des Standortes Pullach. https://publikationen.bibliothek.kit.edu/1000177808. Accessed 23 Apr 2025

Fei F, Costa A, Dolbow JE et al (2023) A phase-field model for hydraulic fracture nucleation and propagation in porous media. Int J Numer Anal Methods Geomech 47:3065–3089. https://doi.org/10.1002/nag.3612

Foulger GR, Wilson MP, Gluyas JG et al (2018) Global review of human-induced earthquakes. Earth Sci Rev 178:438–514. https://doi.org/10.1016/j.earscirev.2017.07.008

Freund LB (1998) Dynamic Fracture Mechanics

Gabriel A-A, Kurapati V, Niu Z, et al (2025) SeisSol. Zenodo

Galis M, Ampuero JP, Mai PM, Cappa F (2017) Induced seismicity provides insight into why earthquake ruptures stop. Sci Adv 3:eaap7528. https://doi.org/10.1126/sciadv.aap7528

Gaucher E, Schoenball M, Heidbach O et al (2015) Induced seismicity in geothermal reservoirs: a review of forecasting approaches. Renew Sustain Energy Rev 52:1473–1490. https://doi.org/10.1016/j.rser.2015.08.026

Gaucher E, Egert R (2022) Statisches Geomechanisches Modell: Schäftlarnstraße, Pullach, Baierbrunn. https://publikationen.bibliothek.kit.edu/1000177807. Accessed 13 Jul 2025

Ge S, Saar MO (2022) Review: induced seismicity during geoenergy development—a hydromechanical perspective. J Geophys Res Solid Earth 127:e2021JB023141. https://doi.org/10.1029/2021JB023141

Geuzaine C, Remacle J-F (2009) Gmsh: a 3-D finite element mesh generator with built-in pre- and post-processing facilities. Int J Numer Methods Eng 79:1309–1331. https://doi.org/10.1002/nme.2579

Gholami Korzani M, Held S, Kohl T (2020) Numerical based filtering concept for feasibility evaluation and reservoir performance enhancement of hydrothermal doublet systems. J Pet Sci Eng 190:106803. https://doi.org/10.1016/j.petrol.2019.106803

Han Z, Ren G, Younis RM (2023) Automatic time step control to resolve hydromechanically driven fault reactivation, spontaneous nucleation, and seismic arrest. Water Resour Res 59:e2023WR035626. https://doi.org/10.1029/2023WR035626

Han Z, Ren G, Younis RM (2021) Unified Reservoir And Seismic Simulation With Explicit Representation Of Fractures And Faults. OnePetro

Harris RA, Barall M, Aagaard B et al (2018) A suite of exercises for verifying dynamic earthquake rupture codes. Seismol Res Lett 89:1146–1162. https://doi.org/10.1785/0220170222

He M, Li Q, Li X (2022) A new simulator for hydromechanical coupling analysis of injection-induced fault activation. Geomech Geophys Geo-Energ Geo-Resour 8:43. https://doi.org/10.1007/s40948-022-00353-x

Heinecke A, Breuer A, Rettenberger S, et al (2014) Petascale High Order Dynamic Rupture Earthquake Simulations on Heterogeneous Supercomputers. In: SC '14: Proceedings of the International Conference for High Performance Computing, Networking, Storage and Analysis. pp 3–14

Ida Y (1972) Cohesive force across the tip of a longitudinal-shear crack and Griffith's specific surface energy. J Geophys Res 1896–1977(77):3796–3805. https://doi.org/10.1029/JB077i020p03796

INL (2023) INL. In: MOOSE framework—tensor mechanics module. Idaho National Lab. https://mooseframework.inl.gov/modules/tensor_mechanics/index.html.

Jaeger JC, Cook NGW, Zimmermann R (2007) Fundamentals of rock mechanics, 4th edition. Blackwell publishing, Oxford

Jin L, Zoback MD (2018) Fully dynamic spontaneous rupture due to quasi-static pore pressure and poroelastic effects: an implicit nonlinear computational model of fluid-induced seismic events. J Geophys Res Solid Earth 123:9430–9468. https://doi.org/10.1029/2018JB015669

Keilegavlen E, Fumagalli A, Berge R, Stefansson I et al (2019) Implementation of mixed-dimensional models for flow in fractured porous media. In: Radu FA, Kumar K, Berre I (eds) Numerical mathematics and advanced applications ENUMATH 2017. Springer International Publishing, Cham, pp 573–580

Khan S, Khulief YA, Al-Shuhail AA (2020) Effects of reservoir size and boundary conditions on pore-pressure buildup and fault reactivation during CO2 injection in deep geological reservoirs. Environ Earth Sci 79:294. https://doi.org/10.1007/s12665-020-09040-0

Kim K-H, Seo W, Han J et al (2020) The 2017 M.L 54 Pohang earthquake sequence, Korea, recorded by a dense seismic network. Tectonophysics 774:228306. https://doi.org/10.1016/j.tecto.2019.228306

Kivi IR, Pujades E, Rutqvist J, Vilarrasa V (2022) Cooling-induced reactivation of distant faults during long-term geothermal energy production in hot sedimentary aquifers. Sci Rep 12:2065. https://doi.org/10.1038/s41598-022-06067-0

Koch T (2020) Mixed-dimension models for flow and transport processes in porous media with embedded tubular network systems. Eigenverlag des Instituts für Wasser- und Umweltsystemmodellierung der Universität Stuttgart, DoctoralThesis, Stuttgart

Kohl T, Mégel T (2007) Predictive modeling of reservoir response to hydraulic stimulations at the European EGS site Soultz-sous-Forêts. Int J Rock Mech Min Sci 44:1118–1131. https://doi.org/10.1016/j.ijrmms.2007.07.022

Kolditz O, Bauer S, Bilke L et al (2012) OpenGeoSys: an open-source initiative for numerical simulation of thermo-hydro-mechanical/chemical (THM/C) processes in porous media. Environ Earth Sci 67:589–599. https://doi.org/10.1007/s12665-012-1546-x

Kosack C, Vogt C, Rath V, Marquart G (2010) Stochastic Estimates of the Permeability Field of the Soultz-sous-Forêts Geothermal Reservoir—Comparison of Bayesian Inversion, MC Geostatistics, and EnKF Assimilation. 12:

Kraft T, Deichmann N (2014) High-precision relocation and focal mechanism of the injection-induced seismicity at the Basel EGS. Geothermics 52:59–73. https://doi.org/10.1016/j.geothermics.2014.05.014

Krenz L, Uphoff C, Ulrich T, et al (2021) 3D acoustic-elastic coupling with gravity: the dynamics of the 2018 Palu, Sulawesi earthquake and tsunami. In: Proceedings of the International Conference for High Performance Computing, Networking, Storage and Analysis. Association for Computing Machinery, New York, NY, USA, pp 1–14

Lukas Krenz, Carsten Uphoff, Thomas Ulrich, et al (2021) 3D acoustic-elastic coupling with gravity: the dynamics of the 2018 Palu, Sulawesi earthquake and tsunami. In: SC'21: The International Conference for High Performance Computing, Networking, Storage, and Analysis. St. Louis, MO. ACM, New York, NY, USA, p 13 pages

Lei H, Niemeijer AR, Zhou Y, Spiers CJ (2024) Frictional properties of natural granite fault gouge under hydrothermal conditions: a case study of strike-slip fault from Anninghe fault zone, Southeastern Tibetan plateau. J Geophys Res Solid Earth 129:e2024JB028760. https://doi.org/10.1029/2024JB028760

Liu W, Manga M (2009) Changes in permeability caused by dynamic stresses in fractured sandstone. Geophys Res Lett. https://doi.org/10.1029/2009GL039852

Madariaga R (1976) Dynamics of an expanding circular fault. Bull Seismol Soc Am 66:639–666

Mahmoodpour S, Singh M, Turan A et al (2022) Simulations and global sensitivity analysis of the thermo-hydraulic-mechanical processes in a fractured geothermal reservoir. Energy 247:123511. https://doi.org/10.1016/j.energy.2022.123511

Majer EL, Baria R, Stark M et al (2007) Induced seismicity associated with enhanced geothermal systems. Geothermics 36:185–222. https://doi.org/10.1016/j.geothermics.2007.03.003

Manga M, Beresnev I, Brodsky EE et al (2012) Changes in permeability caused by transient stresses: field observations, experiments, and mechanisms. Rev Geophys. https://doi.org/10.1029/2011RG000382

McGarr A, Simpson D, Seeber L (2002) Case histories of induced and triggered seismicity. In: Lee WHK, Kanamori H, Jennings PC, Kisslinger C (eds) International handbook of earthquake and engineering seismology. Academic Press, pp 647–661

Meng C (2017) Benchmarking Defmod, an open source FEM code for modeling episodic fault rupture. Comput Geosci 100:10–26. https://doi.org/10.1016/j.cageo.2016.11.014

Moein MJA, Langenbruch C, Schultz R et al (2023) The physical mechanisms of induced earthquakes. Nat Rev Earth Environ 4:847–863. https://doi.org/10.1038/s43017-023-00497-8

Mosconi F, Tinti E, Casarotti E et al (2025) Modeling the 3D dynamic rupture of microearthquakes induced by fluid injection. J Geophys Res Solid Earth 130:e2024JB029621. https://doi.org/10.1029/2024JB029621

Muir Wood D (1990) Soil behaviour and critical state soil mechanics. Cambridge University Press, Cambridge [England] ; New York

Paap B, Kraaijpoel D, Wassing B, van Wees J-D (2020) Simulation of induced seismic ground motions using coupled geomechanical and seismic wave propagation models. Geophys J Int 220:1284–1299. https://doi.org/10.1093/gji/ggz506

Palgunadi KH, Gabriel A, Ulrich T et al (2020) Dynamic fault interaction during a fluid-injection-induced earthquake: the 2017 Mw 5.5 Pohang event. Bull Seismol Soc Am 110:2328–2349. https://doi.org/10.1785/0120200106

Pandey SN, Vishal V (2017) Sensitivity analysis of coupled processes and parameters on the performance of enhanced geothermal systems. Sci Rep 7:17057. https://doi.org/10.1038/s41598-017-14273-4

Park J-W, Song J-J (2009) Numerical simulation of a direct shear test on a rock joint using a bonded-particle model. Int J Rock Mech Min Sci 46:1315–1328. https://doi.org/10.1016/j.ijrmms.2009.03.007

Pelties C, Gabriel A-A, Ampuero J-P (2014) Verification of an ADER-DG method for complex dynamic rupture problems. Geosci Model Dev 7:847–866. https://doi.org/10.5194/gmd-7-847-2014

Permann CJ, Gaston DR, Andrš D et al (2020) MOOSE: enabling massively parallel multiphysics simulation. SoftwareX 11:100430. https://doi.org/10.1016/j.softx.2020.100430

Podgorney R, Finnila A, Simmons S, McLennan J (2021) A reference thermal-hydrologic-mechanical native state model of the Utah FORGE enhanced geothermal site. Energies 14:4758. https://doi.org/10.3390/en14164758

Pruess K, Oldenburg CM, Moridis G (1999) TOUGH2 User's Guide, Version 2.0. Lawrence Berkeley National Laboratory, Berkeley, California and USA

Rudnicki JW (1986) Fluid mass sources and point forces in linear elastic diffusive solids. Mech Mater 5:383–393. https://doi.org/10.1016/0167-6636(86)90042-6

Rutqvist J (2011) Status of the TOUGH-FLAC simulator and recent applications related to coupled fluid flow and crustal deformations. Comput Geosci 37:739–750. https://doi.org/10.1016/j.cageo.2010.08.006

Rutqvist J, Oldenburg C (2007) Analysis of cause and mechanism for injection-induced seismicity at the Geysers Geothermal Field. Lawrence Berkeley National Laboratory, California

Rutqvist J, Rinaldi AP, Cappa F, Moridis GJ (2015) Modeling of fault activation and seismicity by injection directly into a fault zone associated with hydraulic fracturing of shale-gas reservoirs. J Petrol Sci Eng 127:377–386. https://doi.org/10.1016/j.petrol.2015.01.019

Savvatis A, Steiner U, Krzikalla F et al (2019) 4D-geomechanical simulations (VISAGETM) to evaluate potential stress relocation in a geothermal targeted fault system in Munich (South Germany). European Geothermal Congress. Den Haag, The Netherlands, pp 11–14

Schmittbuhl J, Lambotte S, Lengliné O et al (2021) Induced and triggered seismicity below the city of Strasbourg, France from November 2019 to January 2021. C R Geosci 353:1–24. https://doi.org/10.5802/crgeos.71

Shan K, Zheng Y, Zhang Y et al (2023) Effects of different fracture parameters on microseisms induced by hydraulic fracturing. Bull Eng Geol Environ 82:231. https://doi.org/10.1007/s10064-023-03240-1

Shi Z, Day SM (2013) Rupture dynamics and ground motion from 3-D rough-fault simulations. J Geophys Res Solid Earth 118:1122–1141. https://doi.org/10.1002/jgrb.50094

Song Y, Jun S, Na Y et al (2023) Geomechanical challenges during geological CO2 storage: a review. Chem Eng J 456:140968. https://doi.org/10.1016/j.cej.2022.140968

Stricker K, Egert R, Schill E, Kohl T (2024) Risk of surface movements and reservoir deformation for high-temperature aquifer thermal energy storage (HT-ATES). Geotherm Energy 12:4. https://doi.org/10.1186/s40517-024-00283-9

Taufiqurrahman T, Gabriel A-A, Ulrich T et al (2022) Broadband dynamic rupture modeling with fractal fault roughness, frictional heterogeneity, viscoelasticity and topography: the 2016 Mw 6.2 Amatrice, Italy earthquake. Geophys Res Lett 49:e2022GL098872. https://doi.org/10.1029/2022GL098872

Uenishi K, Rice JR (2003) Universal nucleation length for slip-weakening rupture instability under nonuniform fault loading. J Geophys Res Solid Earth. https://doi.org/10.1029/2001JB001681

Uenishi K (2009) On the mechanical destabilization of a three-dimensional displacement- softening plane of weakness

Uphoff C, Rettenberger S, Bader M, et al (2017) Extreme scale multi-physics simulations of the tsunamigenic 2004 sumatra megathrust earthquake. In: Proceedings of the International Conference for High Performance Computing, Networking, Storage and Analysis. Association for Computing Machinery, New York, NY, USA, pp 1–16

Uphoff C, Krenz L, Ulrich T, et al (2024) SeisSol

Valley B, Evans KF (2007) Stress state at Soultz-sous-Forêts to 5 km depth from wellbore failure and hydraulic observations. In: SEG Annual Meeting

Vermeer PA (1998) Non-associated plasticity for soils, concrete and rock. In: Herrmann HJ, Hovi J-P, Luding S (eds) Physics of dry granular media. Springer Netherlands, Dordrecht, pp 163–196

Viesca RC (2016) Stable and unstable development of an interfacial sliding instability. Phys Rev E 93:060202. https://doi.org/10.1103/PhysRevE.93.060202

Viesca RC, Garagash DI (2015) Ubiquitous weakening of faults due to thermal pressurization. Nature Geosci 8:875–879. https://doi.org/10.1038/ngeo2554

Walker RL, Knepley MG, Aagaard BT, Williams CA (2023) Multiphysics modelling in PyLith: poroelasticity. Geophys J Int 235:2442–2475. https://doi.org/10.1093/gji/ggad370

Watanabe N, Wong L, Blöcher G, et al (2012) Finite element method for simulating coupled thermo-hydro-mechanical processes in

discretely fractured porous media and application to enhanced geothermal reservoir analysis
Wolf S, Gabriel A-A, Galis M et al (2025) Three-dimensional wave propagation and earthquake dynamic rupture simulations in complex poroelastic media. Geophys J Int 242:ggaf184. https://doi.org/10.1093/gji/ggaf184
Xu B, Xu T, Heap MJ et al (2024a) An adaptive phase field approach to 3D internal crack growth in rocks. Comput Geotech 173:106551. https://doi.org/10.1016/j.compgeo.2024.106551
Xu B, Xu T, Xue Y et al (2024b) Phase field modeling of mixed-mode crack in rocks incorporating heterogeneity and frictional damage. Eng Fract Mech 298:109936. https://doi.org/10.1016/j.engfracmech.2024.109936
Xu B, Xu T, Baktheer A et al (2026) An energy-based dual phase-field model for shear cracking patterns in heterogeneous geomaterials. Eng Fract Mech 332:111774. https://doi.org/10.1016/j.engfracmech.2025.111774
Yan G, Busch B, Egert R, et al (2022) Transport mechanisms of hydrothermal convection in faulted tight sandstones
Yin Z, Huang H, Zhang F et al (2020) Three-dimensional distinct element modeling of fault reactivation and induced seismicity due to hydraulic fracturing injection and backflow. J Rock Mech Geotech Eng 12:752–767. https://doi.org/10.1016/j.jrmge.2019.12.009
Zhang L, Dieudonné A-C, Daniilidis A et al (2025) Thermo-hydromechanical modeling of geothermal energy systems in deep mines: uncertainty quantification and design optimization. Appl Energy 377:124531. https://doi.org/10.1016/j.apenergy.2024.124531